Highlights

- Propagation of disbond damage in composite joints was investigated by experimental testing and numerical modelling.
- Bonded lap joints contained either cohesive or adhesive disbond damage representing manufacturing defects or accidental damage in service.
- A normalised strain energy release rate can establish a master curve of the material fatigue debonding growth rate, covering all the single and mixed modes.
- Using the master curve and calculated debonding driving force, predicted fatigue life covers the upper and lower bounds of test measurement.

Experimental and numerical study of the effects of process-induced disbond on fatigue debonding in composite joints

Yiding Liu[a], Xiang Zhang[a,*], Stuart Lemanski[a], Hamed Yazdani Nezhad[b], David Ayre[b]

[a] Faculty of Engineering, Environment and Computing, Coventry University, CV1 5FB, United Kingdom

[b] Enhanced Composites and Structures Centre, School of Aerospace, Transport and Manufacturing, Cranfield University, MK43 0AL, United Kingdom

[*] Corresponding author. Email address: xiang.zhang@coventry.ac.uk

Abstract

Laboratory coupon joints for fatigue debonding tests usually have narrow width and a through-width initial disbond. However, realistic structural joints are much wider and may contain process-induced defects and accidental damage; both are much smaller than the joint width. Small and discrete damage may behave differently from the idealised through-width disbond crack. This has brought a question on whether the laboratory coupon joint can accurately represent the fatigue behaviour of wider structural joints. This paper presents an experimental and numerical study of fatigue behaviour of a wide bonded lap joint with a process-induced defect of semi-circular shape. Fatigue debonding propagation was monitored by ultrasound inspection. Fatigue life was predicted using a normalised strain energy release rate parameter calculated by finite element method, and the adhesive material fatigue crack growth rate data measured under single and mixed mode conditions. Simulation of process-induced defect and validation by experiments have brought a better understanding of fatigue debonding behaviour in wide joints containing realistic damage. Suggestions are given for fatigue fracture tests of bonded joints.

Keywords: adhesive bonding; disbond; composites; finite element analysis; fatigue life prediction

1. Introduction

The use of adhesive bonded joints in Carbon Fibre Reinforced Polymer (CFRP) composites in the aerospace and civil engineering sectors continues to increase. The benefits of using bonded joints over mechanically fastened joints include weight savings, no stress concentration from fastener holes and more uniform load transfer. To ensure the structural integrity of adhesive bonded joints, accurate prediction of fatigue crack growth rate and life is required; relationship of fatigue crack growth life vs. service load history is used to determine the inspection regimes. However, process-induced defects and accidental damage can have different shapes and in different locations [1], all of which affect the joint integrity [2] and

prediction accuracy. Variations of the adhesive damage modes (adhesion or cohesion failure, and combinations of them) also pose challenges to the predictive models.

Most of the laboratory tests were contemplated on coupon size joints (e.g. 25 mm width) with a starter disbond of through-width strip shape. De Moura et al. [3] studied composite lap joint finding that the joint strength was not affected by a strip disbond located in the middle of the joint overlap. Karachalios et al. investigated the effect of rectangular and circular disbond shapes located in the middle of the overlap on the static strength of steel joints [4]. In the case of small disbond, the shape of disbond does not affect the strength; as the disbond size gets bigger, more rapid decrease in the joint strength is found. Guo et al. analysed the effects of through-width disbond at three different locations on the failure strength and failure mode of composite single lap joints, and found that disbond at the edge of the joint overlap region changes the damage initiation pattern, whereas disbond located at quarter of the lap length accelerated the damage growth to the lap edge [5]. Sahoo et al. studied fatigue debonding of an aluminium joint with a strip disbond of 3 mm width at one end of the bond overlap [6]. Fatigue crack growth rate (FCGR) was predicted using the strain energy release rate (SERR) calculated by finite element analysis (FEA). Elhannani et al. investigated the effect of position, number and shape of adhesive disbond on the shear stress distribution in the adhesive layer by finite element modelling [7]. It is found that when the disbond is in the middle of the overlap, interlaminar shear stresses change little as the stress values here are very low. However, if the disbond is present at the free edge of the bond, it causes very high interlaminar shear stresses. In terms of the disbond shape, circular disbond causes higher stress in the adhesive layer. Therefore, it is more dangerous if a circular disbond exists near the free edges of the bond region.

We have previously studied the fracture behaviour of single lap joints in two configurations: (i) a conventional joint width with a through-width stripe disbond as damage starter, (ii) a wider joint with a semi-circular disbond at the free edge of the bond overlap, where debonding between the adherend and adhesive is likely to occur [8]. In reality, manufacture or service induced damages are unlikely to be through the width of the joint, and the free edge locations are more critical than the middle region. Calculated strain energy release rate distributions along or around the front of a starter damage for the mentioned two joint configurations were calculated as shown in Figure 1, which are very different from each other. For the through-width stripe disbond, normalised mode I and mode II SERR distributions are

almost flat along the defect front apart from sudden jump at the free edges, indicating a uniform crack propagation front. For the semi-circular disbond, the mode I SERR at the crack mouth is much higher that will drive the crack to propagate along the joint width direction first; it can take a long time to propagate the starter defect to the free edges if the width of the joint is sufficiently wide. It is therefore important to develop models to predict wider joint performance under cyclic loads with realistic starter defects in terms of shape and location. So far, to the best knowledge of the authors, there is no published work on the propagation of embedded disbond similar to the configuration of Figure 1(b) for adhesive bonded joints under fatigue loads by experiment or modelling.

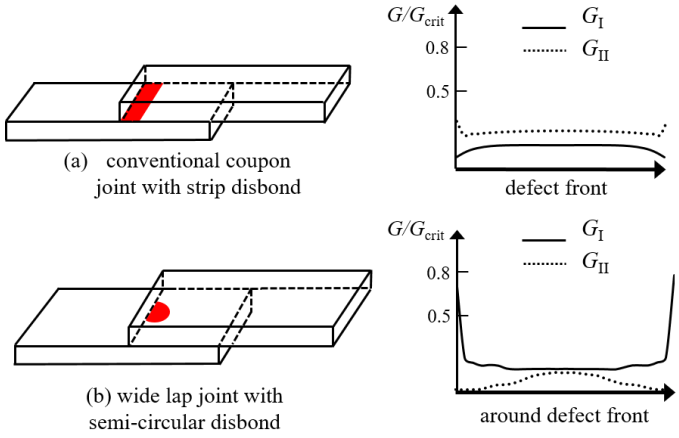

Figure 1: Distribution of SERR for: (a) conventional coupon joint with a through-width strip disbond, and (b) wide lap joint with a semi-circular disbond.

In addition to purposely embedded disbond [3–7], defects can exist inside the adhesive bulk as well as at the adherend-adhesive interface. This paper presents an experimental and numerical investigation of fatigue behaviour of a wide composite lap joint with an idealised disbond starter of semi-circular shape in the adhesive bulk and also at the adherend-adhesive interface. Fatigue testing was conducted and debond propagation was monitored by ultrasound inspection. Fatigue debonding was also modelled in a two-step analysis: a) computing the strain energy release rate by the Virtual Crack Closure Technique (VCCT) under quasi-static load with a crack extension scheme; b) calculating fatigue debonding rate by a normalised strain energy release rate representing the combination of single and mixed modes of the debonding driving force (i.e. SERR) and fatigue debonding growth rate property the adhesive material. Fatigue life is then predicted and compared with experimental results of both conventional and wide coupon joints.

2. Experimental

2.1 Materials and specimens

Composite adherends of 2 mm thickness were manufactured from unidirectional Hexcel® IM7/8552 carbon fibre epoxy pre-preg with quasi-isotropic stacking sequence of $[0/45/90/-45]_S$. The geometry and dimensions of wide lap joint, as shown in Figure 2, were proportionally adopted from ASTM standard D3165 [9]. The adherends were bonded by Cytec FM® 94 modified epoxy adhesive film, which is a moisture resistant adhesive designed for use in high temperature environment. The nominal thickness is 0.25 mm including the polyster carrier cloth. The joints are assembled using secondary bonding process with two cured composite plates curing with the adhesive together. An artificial disbond of semi-circular shape was cut off from a 0.025 mm thickness Teflon® release film using a circular punch and embedded in the front. To ensure high surface quality during the bonding process, a coupled surface treatment was used; application of peel ply followed by pre-treatment with Onto™ SB 1050 supplied by Oxford Advanced Surfaces [10] to introduce chemical bonding interactions, since peel ply alone cannot ensure a perfect quality bond and may not necessarily satisfy initial airworthiness requirements [11–14]. The joint specimens were cured at 120 ºC for 40 minutes. A constant pressure of 0.28 MPa was uniformly applied using a clamping plate with fasteners (see Figure 2(c)). Debonding cracks were monitored from the four corners of the joint overlap area, which are denoted as A and B (at the runout end with artificial disbond), C and D (the opposite end without artificial disbond), as shown in Figure 2(b).

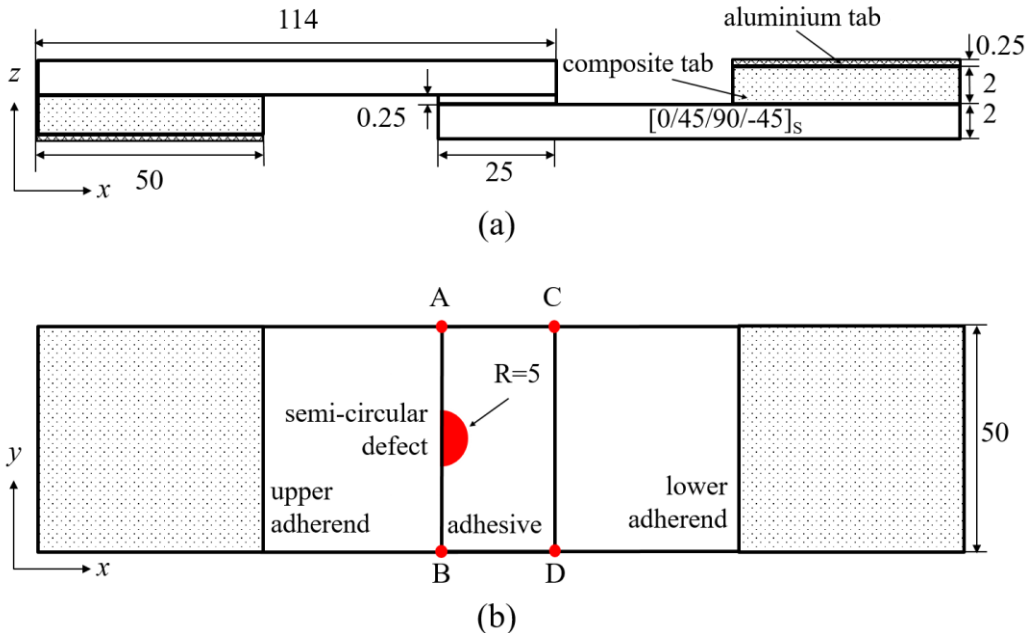

(c) (d)

Figure 2: Wide lap joint used in this study: (a) side view, (b) top view showing a semi-circular initial disbond; geometry and dimensions are adopted from [9] (unit: mm). Fatigue cracks were monitored from the four corners of the adhesive bond, marked as A, B, C, D. (c) clamping plates with fasteners to ensure uniform adhesive thickness, (d) fatigue experiment setup

2.2 Types of initial disbond

Adhesive debonding may be caused by either cohesion failure (fracture within the adhesive bulk) or adhesion failure (interfacial failure between adhesive and adherend) [15]. Cohesion failure found in service is typically a design issue, e.g. insufficient overlap length or excessive peel stress, or excessive porosity, e.g. due to exposure of pre-cured adhesive film to high humidity. Adhesion failure occurs as a direct result of the manufacturing quality, e.g. inappropriate surface preparation or ineffective surface treatment process (a chemically inactive surface).

To replicate these two damage scenarios in laboratory tests, two different types of initial disbond were embedded in the specimens. Adhesive disbond was inserted in the adherend-adhesive interface using one layer of adhesive (referred as "AD specimen", Figure 3(a)). Cohesive disbond was inserted between two adhesive layers (referred as "CD specimen", Figure 3(b)). It is worth noting that the nominal thickness of these specimens was almost the same regardless of adhesive disbond or cohesion disbond as the two adhesive layers were melted into each other during the curing cycle (measured adhesive thickness was 0.37 mm for adhesion disbond (AD) and 0.42 mm for cohesion disbond (CD) after curing). This is considered to be caused by the presence of carrier cloth in the adhesive, which acts as a spacer between the adherends during curing and it is effective at controlling the bondline thickness. Care was taken to ensure that the cohesion disbond remained in the adhesive bulk and not repositioned to the adherend-adhesive interface after the curing process.

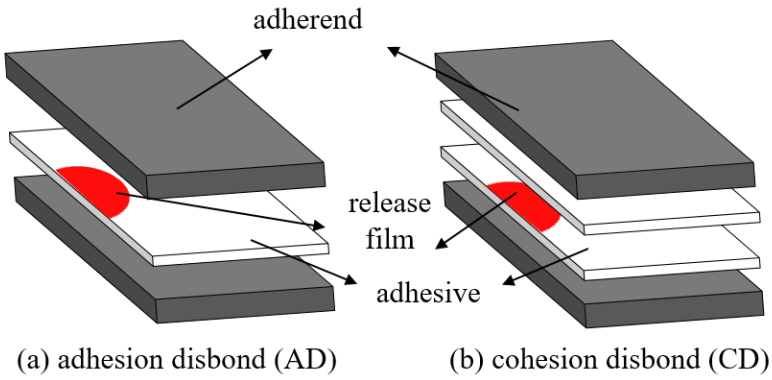

Figure 3: Schematic of designed disbonds: (a) adhesion disbond (AD) inserted at the adhesive-adherend interface, (b) cohesion disbond (CD) embedded between two adhesive layers and cured within the adhesive bulk.

2.3 Fatigue tests and results

Fatigue tests were conducted under constant amplitude load on a DMC servo-hydraulic tester with a 20 kN load cell (see Figure 2(d)). The maximum applied load 8.46 kN was at 50% of the static failure load. The cyclic load ratio was 0.1 and the test frequency was 3 Hz. Two specimens of each disbond type were tested, named as CD-F1, CD-F2 and AD-F1, AD-F2.

2.3.1 Crack growth monitoring

Crack growth was monitored by ultrasound C-scanning at selected test intervals before it reaches the joint free edges. After running test for the initial 3×10^4 cycles, the specimen was removed from the test machine for ultrasound inspection and then realigned to the machine to continue another 5×10^4 cycles. The inspection intervals were adjusted according to the damage propagation observed from previous C-scan. To avoid alteration of realignment, a specimen centreline was marked.

Once the debonding had reached the joint free edge(s), crack lengths were measured from the four corners of the joint overlap (A, B, C, D position in Figure 2) using a travelling optical microscope equipped with a digital camera. To observe the crack profile, fatigue test was interrupted a few times with static tension load being maintained to open the crack, and red ink was manually injected through a needle nozzle through the interface of the overlap. It allows the liquid to flow to the disbond area for post-failure identification of the crack propagation profile. This is similar to the dye penetrant technique used in the aerospace and other industries, which does not influence the crack propagation rate [16].

Figure 4 illustrates ultrasonic C-scan results of (a) adhesion disbond specimen (AD-F1) after 5×10^4, 1×10^5 and 1.7×10^5 cycles, (b) cohesion disbond specimen (CD-F1) after 8×10^4,

1.4×10^5 and 2.4×10^5 cycles compared with the initial disbond profile before testing. The dark red colour indicates strong signal suggesting good bond (the small signal variation in the dark red region is the result of non-uniform adhesive thickness). The black colour typifies the disbond that absorbed all ultrasound signals. Measured crack lengths in the transverse and concentric directions ($2a_1$ and a_2, respectively) are presented in Table 1.

The C-scan results indicate significant scatters in laboratory tests of composite lap joints. By comparing the images taken at various intervals, an evident crack growth in the transverse direction could be observed, which speedily extended to the joint free edges for the adhesion type initial disbond. It can be seen that crack also grew in the concentric direction at the early cycles, although the growth rate is much slower than that in the transverse direction. Similar crack growth pattern was also observed for the cohesion disbond, however, crack propagated gradually in both directions. This suggested that fatigue damage mainly evolves in the transverse direction (i.e. perpendicular to the loading direction) until reaching the joint width.

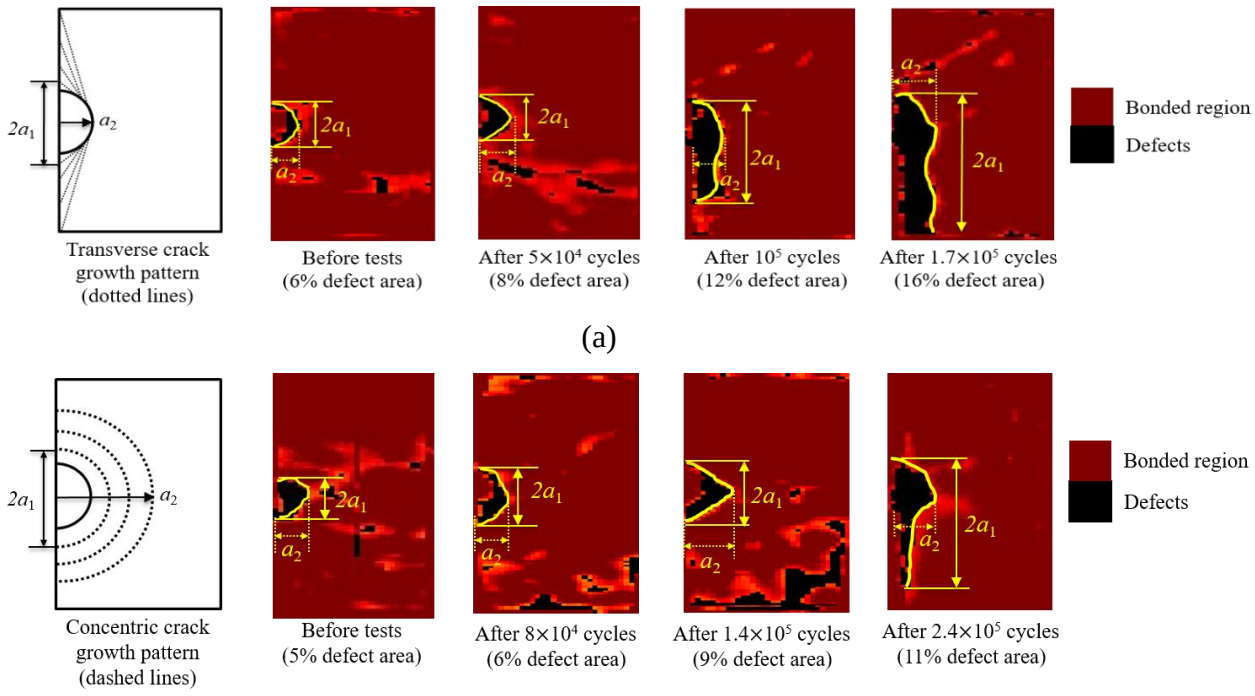

Figure 4: C-scan images of crack growth profiles for (a) adhesion disbond (specimen AD-F1) at 5×10^4, 1×10^5 and 1.7×10^5 load cycles, (b) cohesion debond (CD-F1) at 8×10^4, 1.4×10^5 and 2.4×10^5 cycles.

Table 1 Measured crack lengths in transverse and concentric directions according to C-scan results (unit: mm)

	Adhesion disbond, Specimen F1 (AD-F1)				Cohesion disbond, Specimen F1 (CD-F1)			
	Initial debond size	5×10^4 cycles	1×10^5 cycles	1.7×10^5 cycles	Initial debond size	8×10^4 cycles	1.4×10^5 cycles	2.4×10^5 cycles

Transverse direction ($2a_1$)	9.2	11.2	21.9	29.3	8.5	10.0	11.3	23.5
Concentric direction (a_2)	4.4	5.1	5.3	7.5	4.9	5.2	6.6	6.8

Note: for the transverse and concentric crack profiles, see sketch in Figure 4.

2.3.2 Fatigue crack growth life

Figure 5 plots the monitored crack length (a) measured from four corners (A, B, C, D) with respect to number of cycles (N) for cohesion-disbond ((a) CD-F1 and (b) CD-F2) and adhesion-disbond ((c) AD-F1 and (d) AD-F2) specimens. For all specimens, main cracks were observed from corners A and B, whereas minor cracks were discovered at corners C and D after some period as a result of secondary bending. Crack growth rate was approximately the same for corners A and B, indicating that crack front has already become uniform when the crack could be observed from corners A and B, and later from corners C and D.

Fatigue crack growth rate in composite lap joints show a significant difference between cohesion and adhesion disbonds. The fatigue load cycle curve of the cohesion disbond (CD) is apparently gradual until 6×10^5 to 8×10^5 cycles, while that of the adhesion disbond (AD) is rapid ultimately failing at 4.5×10^5 cycles, representing 40% reduction in fatigue life. Literature also showed significant scatter between the two types of debonding [17], which is one of the main difficulties in implementing a damage tolerance design for adhesive joints. Other published studies [18,19] have suggested that small differences in adhesive thickness have little influence on the fatigue crack growth rate. Therefore, it is reasonable to suggest that the large difference in the fatigue behaviour is related to the different types of disbond starter; crack resulting from cohesion disbond propagates via the cohesion failure mechanism (i.e. fracture within the adhesive layer in the plane of the carrier cloth), as shown in Figure 6(a). In adhesion disbond scenario, it is easier to have an adhesion failure as the starter disbond was inserted between the adherend-adhesive interface, consequently it would require higher energy to propagate into the adhesive bulk causing cohesive failure. This was also observed in the cohesion disbond specimens as the fabric carrier deflected the internal cracks towards the interfaces. However, with the cohesion disbond, theoretically, both cohesion failure and adhesion failure can occur. As the resistance to cohesion failure is much greater than that to adhesion failure, observed damage mode switch during fatigue testing is understandable, i.e., a cohesive crack deviated towards to the adherend-adhesive interface. With this failure mode switch from cohesion to adhesion in the CD specimen, crack would

require higher strain energy to propagate, hence larger number of load cycles comparing to the adhesion disbond specimens.

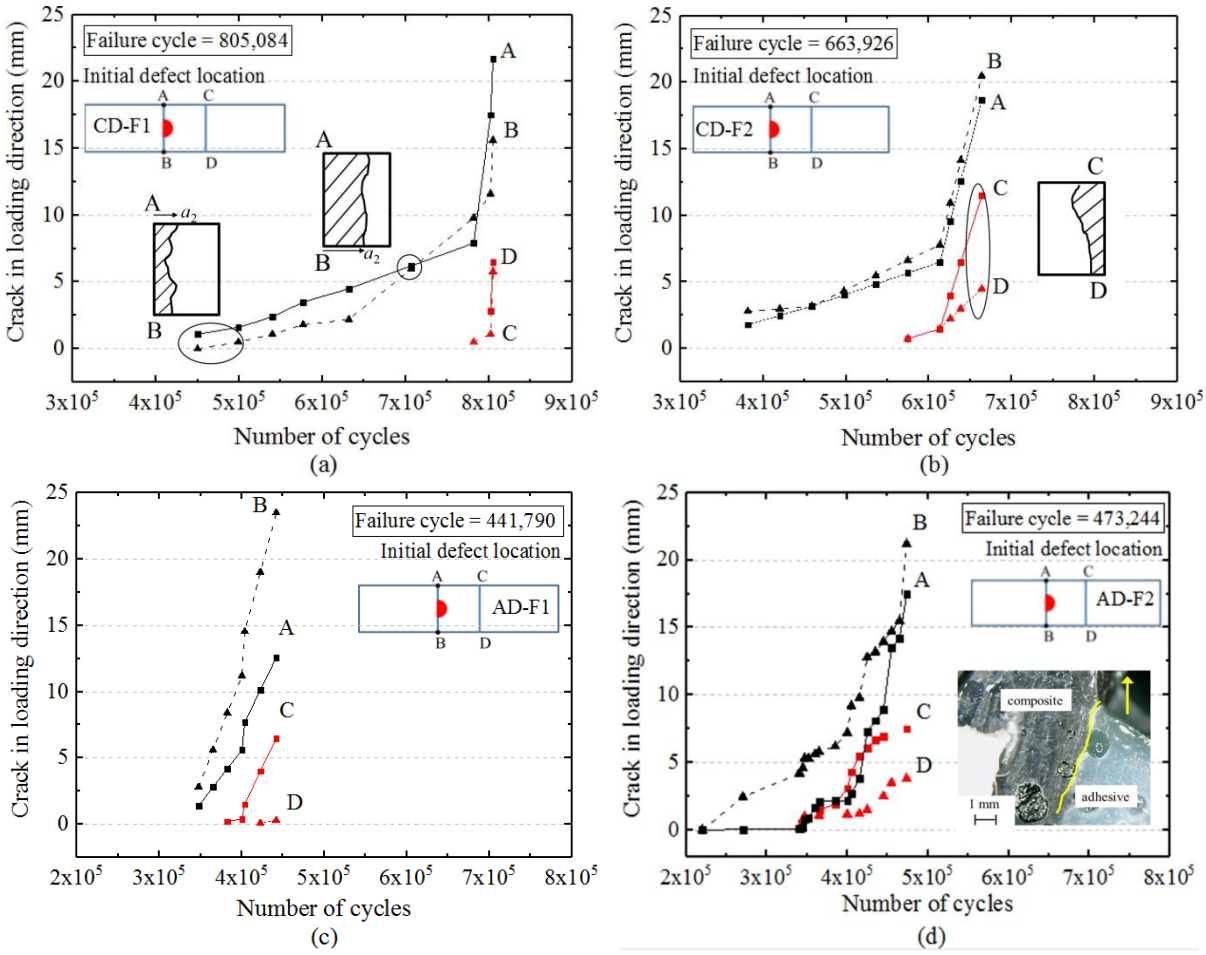

Figure 5: crack lengths in the load direction measured at four corners of overlap (A,B,C,D; a_2 is the main crack from artificial disbond); (a) and (b) show cohesion disbond specimens CD-F1 and CD-F2, (c) and (d) show adhesion disbond AD-F1 and AD-F2; photo insert shows crack from A and B at the maximum cyclic load at 381,718 cycles, yellow line indicates crack propagation path, and arrow points the applied load direction.

2.3.3 Fractography

Fractographic examination was carried out after fatigue testing. Figure 6(a) shows the fracture surfaces of a cohesion disbond specimen (CD-F2) with red ink marked interface. The left interface represents the crack propagation after 541,876 cycles. The shape of the ink mark supports the assertion that the crack front has rapidly elongated to the joint free edges and that by this stage the crack has become a uniform full-width disbond of about 9 mm length. A mixed adhesion-cohesion failure was observed for CD-F2. Fractography of adhesion disbond specimen (AD-F2) without red ink insertion is shown in Figure 6(b) illustrating adhesion failure dominance. Delamination in adherend is also observed in AD-F2.

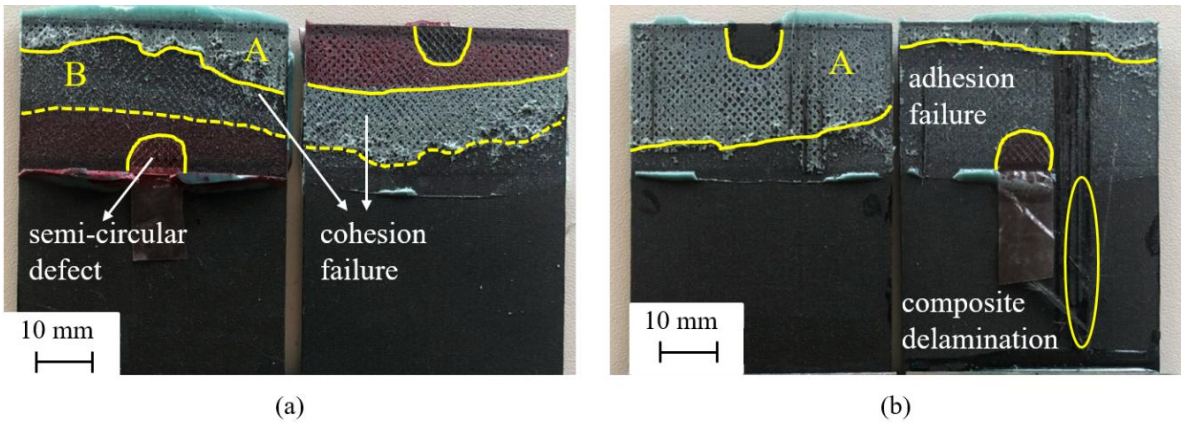

Figure 6: Fracture surfaces of (a) cohesive disbond specimen (CD-F2) in mixed adhesion-cohesion failure; red ink indicates a full-width crack of 9 mm at 541,876 cycles, (b) adhesion disbond specimen (AD-F2), adhesion failure and delamination were observed. Area A is cohesion failure and B is adhesion failure.

2.4 Fatigue crack growth rate property for FM94 adhesive

Predicting the fatigue life of joints requires the adhesive material data in terms of debonding crack growth rates under mixed mode load. In this study, the Double Cantilever Beam (DCB, mode I), Mixed Mode Bending (MMB, mixed mode ratio of 0.5 and 0.75 as defined in Eq. (1)) and three-point End Notch Flexure (ENF, mode II) geometries bonded with the FM®94 adhesive were tested, as shown in Figure 7. The initial disbond was always at the adhesive-adherend interface. Fatigue crack growth rate (FCGR) was calculated from measured a vs. N relation using the 7-point incremental polynomial method in accordance with the ASTM Standard E647 [20]. Our test data are compared with published work in [21], where fatigue tests were conducted on lap joints made of aluminium adherends and FM®94 adhesive under the modes I, II and mixed mode ratio of 0.25 and 0.75.

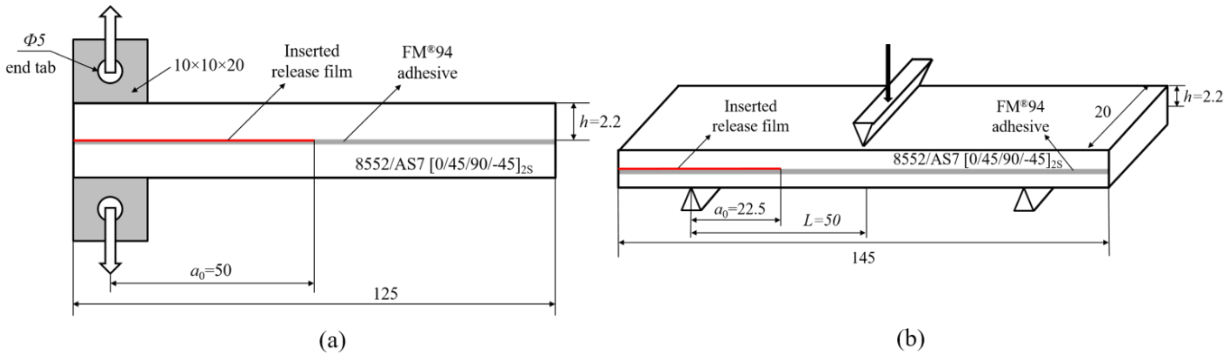

Figure 7: Dimensions, materials and layup for DCB and three-point ENF specimens (unit: mm). Disbond starter was inserted at the adherend-adhesive interface.

The Paris law type relation based on fracture mechanics has been widely used in the fatigue delamination studies for composites [22] and adhesive joints [23,24]. There is no general consensus on the similitude parameter governing fatigue delamination/disbond growth rate.

Discussion on the importance of using an appropriate governing parameter was made in a previous study by the author [25]. In this current study, a normalised parameter, g_{max}, is used as defined in Eq. (2). It takes account of the effect of the fracture toughness (G_{IC} and G_{IIC}) to reduce the scatter in the fatigue crack growth rate data. The Paris law in Eq. (3) is represented accordingly in Eq. (4):

$$r = \frac{G_{II}}{G_I + G_{II}} \tag{1}$$

$$g_{\max} = \frac{G_{I,\max}}{G_{IC}} + \frac{G_{II,\max}}{G_{IIC}} \tag{2}$$

$$\frac{da}{dN} = C\left(G_{\max}\right)^m \tag{3}$$

$$\frac{da}{dN} = C'\left(g_{\max}\right)^{m'} \tag{4}$$

where $G_{IC,}$ G_{IIC} are the static delamination toughness, also known as the critical strain energy release rate, in mode I and II respectively, C and m are the coefficient and exponent of the traditional Paris law [26], C' and m' are modified Paris law parameters that are determined by fitting the test data.

Figure 8(a) shows measured FCGR of FM®94 adhesive vs. the maximum SERR (G_{max}) measured from single mode and mixed mode coupons. A distinct difference exists between the mode I and mode II, and the fatigue debonding rate data are divided into three zones: mode I dominant (r = 0~0.5), mixed mode (r = 0.5~0.8) where majority data points are inclined to pure mode I, and mode II dominant (r = 0.8~1). Figure 8(b) shows the scanning electron microscope (SEM) images of the fracture surfaces associated with (i) mode I, (ii) mixed mode ratio of 0.5 and (iii) mode II failures of FM®94 adhesive bonded with aluminium substrates [21,27]. For mode I debonding, the micro cracks grow in different directions ahead of the crack tip, and then coalesced to form a main crack. Mode II fracture surfaces contain mainly rollers and vertical cracks. For the mixed mode loading (ratio 0.5), the fracture surface feature is similar to that of the mode I, which substantiates the disbond growth rate being closer to the pure mode I result. The mixed mode behaviour is strongly influenced by the presence of the fibre carrier cloth in FM94, which has higher resistance to the mode II loads, resulting in a reduced mode II fracture than that imposed upon the samples (i.e. by the secondary bending effect).

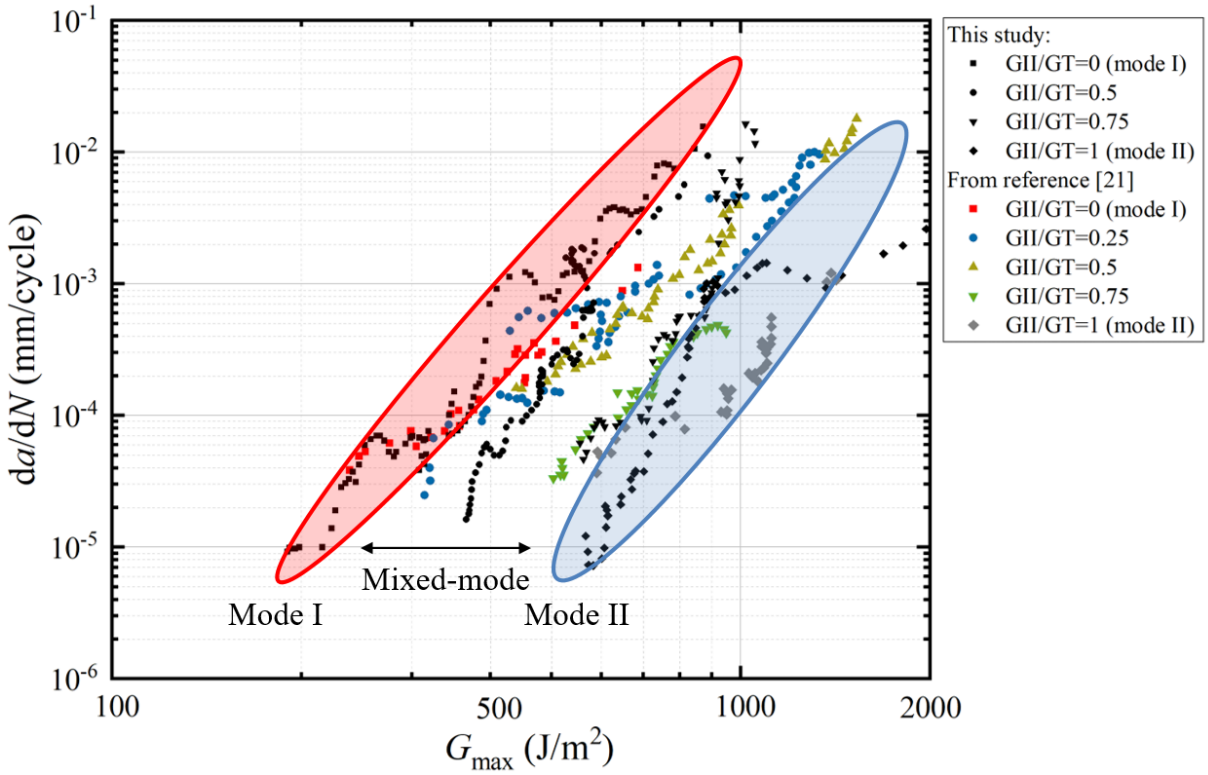

Figure 8(a): Measured fatigue crack growth rate vs. maximum SERR (G_{max}) for FM94 adhesive; filled symbols indicate adhesion debonding by authors of this paper; filled symbols represent cohesion debonding taken from reference [21], using the same adhesive material with aluminium adherends and with initial disbond at the adherend-adhesive interface. G_{max} was calculated using the modified beam theory in [28] at the maximum load with displacement control.

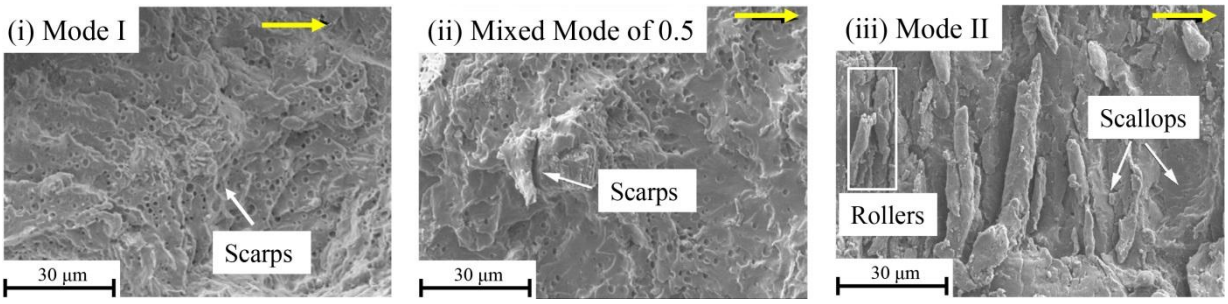

Figure 8(b): Microscopic photos of fracture surfaces of (i) mode I, (ii) mixed mode of ratio 0.5, (iii) mode II, of FM94 with aluminium adherends, adopted from [21]; white arrows indicate characteristics related to different modes; yellow arrows indicate the main crack growth direction.

Figure 9 shows modified plots of FCGR vs. normalised maximum SERR for the same fatigue data as shown in Fig. 8a. For this particular adhesive, it can be seen that majority of the test data at different modes can be covered by a ±35% scatter band so that the best fitted curve can be regarded as a "master curve" that can be described by the Paris law. This linear curve is also a good fit for the pure mode I data in this graph, which may explain why some studies

have used just the mode I data to predict mixed mode crack propagation rate in composite joints [29,30].

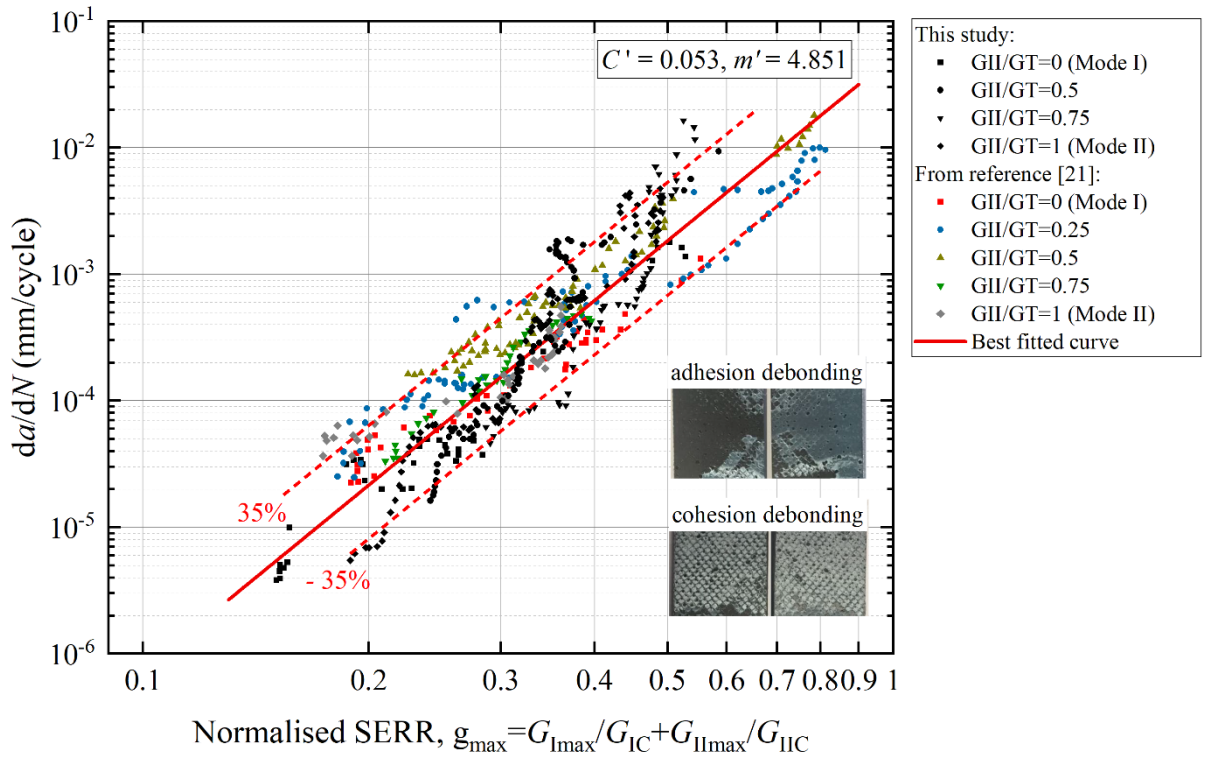

Figure 9: Fatigue crack growth rate vs. normalised SERR (Eq. (2)) of FM94 adhesive for mixed mode tests. Black filled symbols represent adhesion debonding; colour filled symbols are cohesion debonding taken from [21]; red line is the best fitted curve of all test data including data from [21]. Toughness values used: $G_{IC\ (adhesion)}$=867 J/m^2, $G_{IC\ (cohesion)}$=1420 J/m^2, $G_{IIC\ (adhesion)}$=2955 J/m^2, $G_{IIC\ (cohesion)}$=3462 J/m^2, from this study and references [18,21]. Upper and lower boundaries (dash lines) are parallel with the best fitted curve covering majority data points.

3 Modelling approach

3.1 FE model of crack extension

Figure 10 shows the load and boundary conditions of a wide lap joint with a semi-circular disbond. Both the adherends and adhesive were modelled by linear brick elements with incompatible mode (denoted as element C3D8I in ABAQUS code) to enhance the accuracy of bending behaviour. Crack extension was modelled under quasi-static load condition by manually releasing the crack tip nodes in the adherend-adhesive interface and modifying the bonded node set according to a designated pattern. Mesh size of 0.5 mm was used in the bond region based on mesh convergence study. The SERR components were computed using the crack tip node forces and crack opening displacement behind the crack tip. The implicit integration is suitable for debond modelling for computational efficiency and convergence.

By running several FE analyses with different crack lengths and corresponded crack growth profiles, variation of SERR with respect to crack growth profile were calculated.

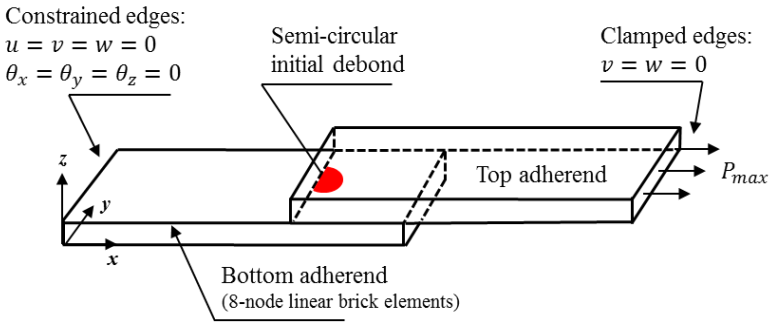

Figure 10: Load and boundary conditions of a wide joint with a semi-circular disbond; the left end were fully constrained, the right end is simply supported with free movement in the x-axis and subjected to a load.

3.2 Strain energy release rate (SERR)

Crack length along the transverse direction before reaching the free edges was defined as a_1. After reaching the free edges, it propagated along the overlap length direction, which was defined as a_2, as shown in Figure 11(a). FE modelling of selected continuous crack growth profiles (a_1 of 5, 6.5, 10.2, 12.4, 17.9 and 20.8 mm based on C-scanning) were performed and the mode I, II and III SERR components (G_{I}, G_{II} and G_{III}) at the crack tip locations were illustrated in Figure 11(b). The assumption of crack propagation along the 0° direction is based on the ratio of the total SERRs at two crack fronts in 0° and 90° directions as the C-scan revealed much slower crack propagation along the concentric directions.

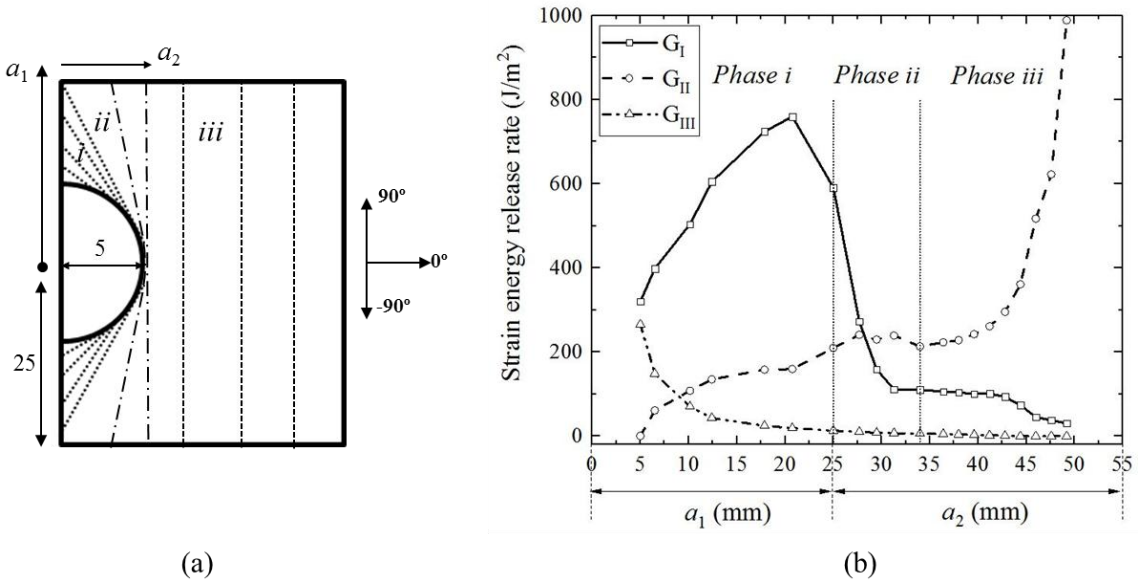

Figure 11: (a) Definition of crack growth profile in three phases (*i*, *ii*, *iii*) in transverse and concentric patterns (unit: mm), (b) mode I, II and III SERR components (G_{I}, G_{II} and G_{III}) vs. crack length (a_1 and a_2) calculated under static maximum load 8.46 kN.

Figure 11(b) shows that three crack propagation phases can be defined by the fracture mode change. In phase *i* (crack extends towards the free edges), G_I keeps increasing due to the free edge stress concentration at the a_1 crack front. G_{III} component exists at the 90° crack tip during phase *i*, which could not be ignored when the crack length was relatively small as the in-plane tension could bring out-of-plane shear deformation. In phase *ii* (crack transferred to a 5 mm strip crack similar to the initial disbond in narrow coupon joint), crack length grew longer and local stress becomes more perpendicular to the crack plane. G_I dropped significantly from 600 J/m^2 to around 150 J/m^2, but G_{II} was almost constant, indicating the dominant fracture mode switching from mode I to mode II as the joint experienced higher shear stress when the crack reached the free edges. G_{III} becomes much smaller than both G_I and G_{II} and can be neglected from Phase ii onwards. In phase *iii* (uniform crack front), G_{II} increased steeply from 200 J/m^2 to more than 1000 J/m^2, whereas G_I decreased significantly to around 20 J/m^2. The contribution of mode II is more important and eventually the crack becomes unstable causing a sudden failure.

3.3 Fatigue life prediction

Fatigue life prediction procedure used in this study is shown in Figure 12. Three parts are involved: (1) basic material property test including the fracture toughness and Paris law relationships for different mixed modes; (2) calculation of the crack growth driving force (SERR components) by FEA, using the model shown in Figure 9. The obtained SERR was then employed to Eq. (2) taking account of two different scenarios of adhesion or cohesion debonding by using the corresponding facture toughness and the master trend line of the crack growth rate data (Figure 9); (3) predict the fatigue crack growth rate and life by numerically integrating the Paris law using cumulative damage algorithm, starting from the initial crack length to the final critical crack length.

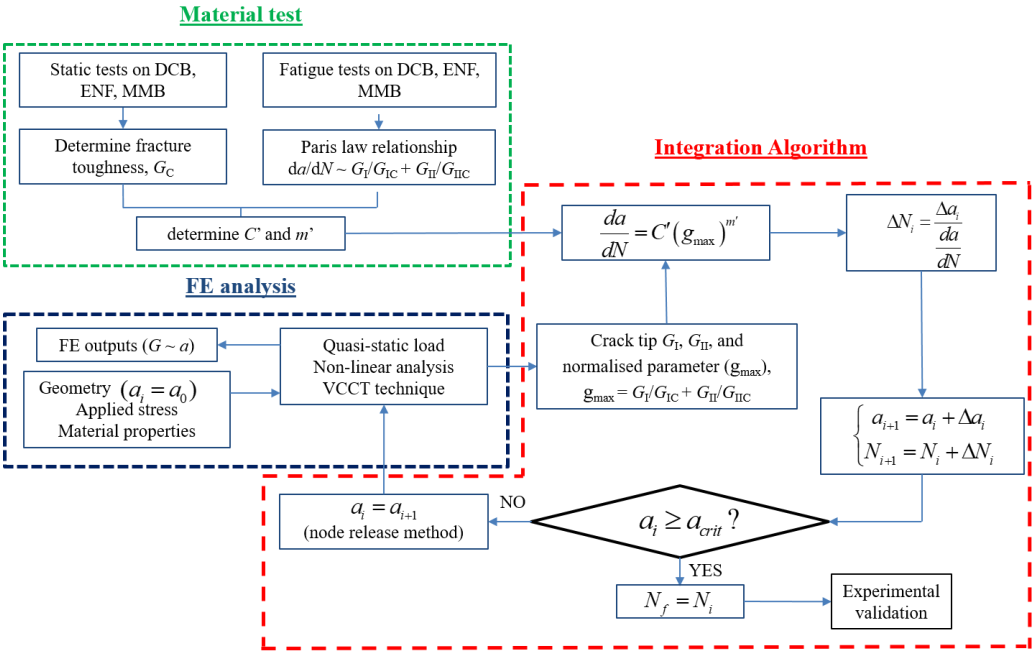

Figure 12: Flow chart of procedures used for fatigue life prediction; three key steps are: material test, FE analysis of crack growth driving force, and numerical integration algorithm for crack growth accumulation.

4 Validation of fatigue life prediction

Predicted crack length (a_1) vs. cycle numbers (N) for the Phase *i* and *iii* and comparison with experimental measurement are presented in Figure 13. For the semi-circular disbond, nearly half of the total fatigue life is spent to propagate the initial disbond to the joint free edges.

In the process of initial disbond propagating to reach the joint width (i.e. Phase *i*), prediction based on cohesion debonding data is more accurate than using the adhesive debonding data, indicating that cohesion damage is the dominant mode in Phase *i*. This model gradually changed into the adhesive debonding mode with further crack propagation, shown by the required larger cycle numbers in the crack prediction, as shown in Figure 13(b) in Phase *iii*). For Phase *iii*, adhesion debonding mode is more efficient compared to cohesion debonding model, indicating the dominance of adhesion failure in this phase.

The cohesion debonding model provides un-conservative life prediction comparing to the adhesion debonding model. This difference could possibly be ascribed to the smaller normalised g_{max} value in the cohesive debonding case due to higher delamination toughness values (G_{IC} and G_{IIC}, see the values in the captions of Figure 9) caused by the carrier cloth, which results in a slower FCGR and longer fatigue life. The adhesion debonding based model has satisfactorily predicted the fatigue life caused by adhesion disbond, whereas the model based on cohesion reproduces the initial stage of the fatigue life of the cohesion disbond more

closely but fails to accurately predict the final failure. This is caused by the cumulative effect of small discrepancies between the experimental tests (Figure 8(a)) and the normalised, fitted data (Figure 9). Therefore, the normalisation to one master trend curve does not accurately predict the fatigue life when the mixed mode ratio is higher than 0.5 in Phase *iii*. However, Phase *iii* is the final stage of crack growth life when the growth rate is faster; therefore, this method still provides qualitative agreement of the behaviour even in these latter stages of crack propagation.

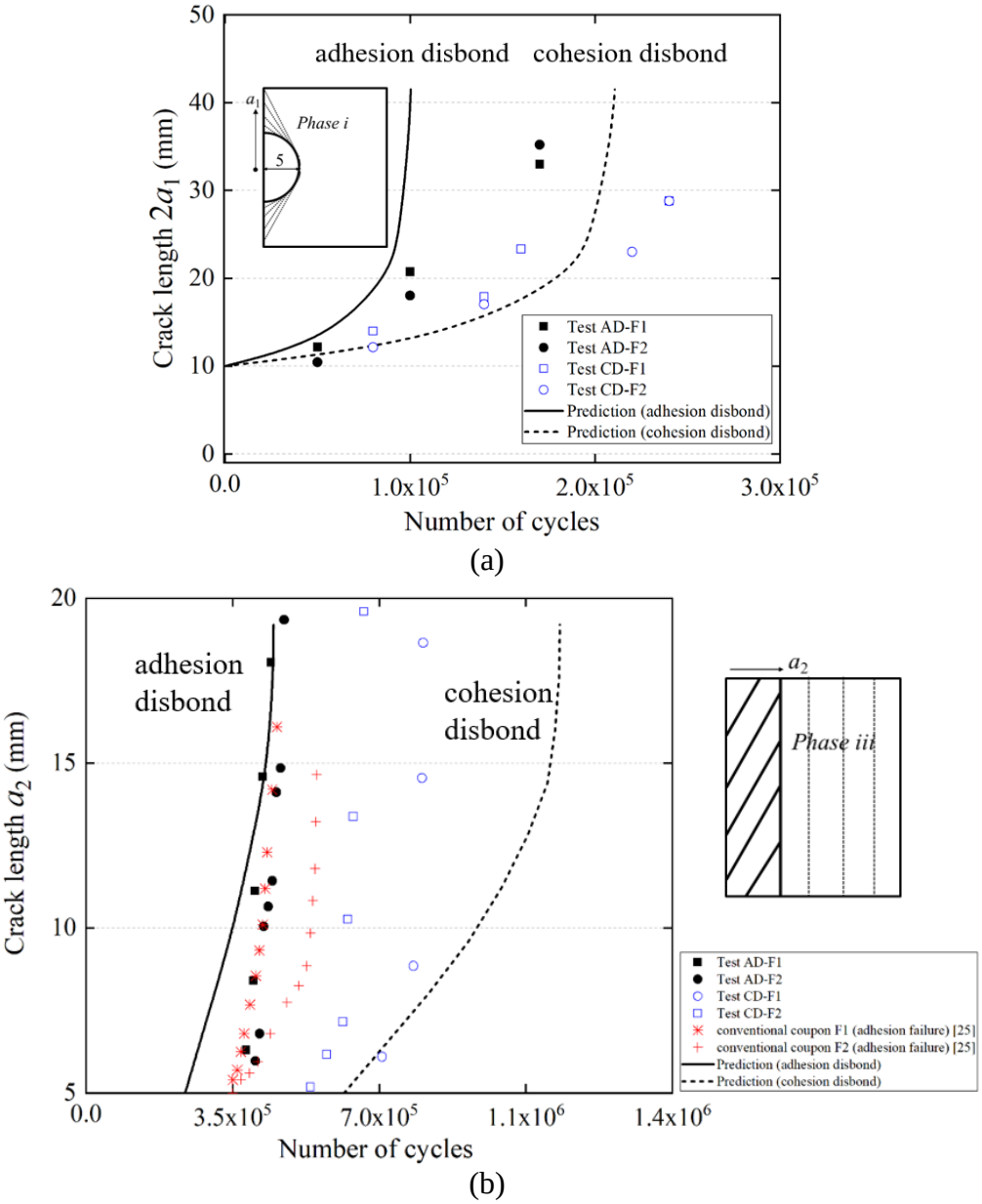

Figure 13: Fatigue crack growth life prediction in (a) Phase *i* (crack configuration a_1) and (b) Phase *iii* (crack configuration a_2), and comparison with test results and conventional coupon joint (adhesion failure) [25].

5 Discussion

The experimental results have shown variations and scatters; for joints with cohesion disbond, fatigue life of the two specimens were 6.7×10^4 and 8.1×10^4 cycles. It is not uncommon in the large scale laboratory fabrication of bonded joints that samples may have localised defects (i.e. due to inappropriate surface preparation or ineffective surface treatment), even though there are bonding quality assurance guidance. Another reason is the porosities and voids in the adhesive, as shown by the Scanning Electron Microscope (SEM) images in the adhesive taken from the adhesion disbond specimen (AD-F2) in Figure 14. Roughly 15% of porosity and void exist in the adhesive (the largest porosity diameter was about 1 mm), which affected the joint fatigue behaviour and caused scatters.

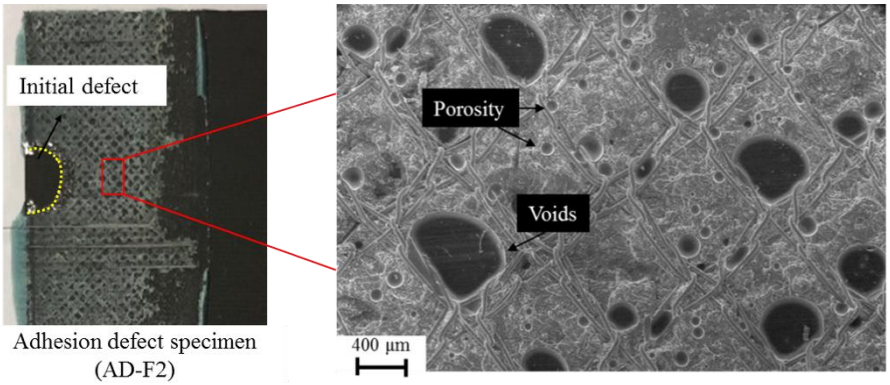

Figure 14: Scanning Electron Microscope (SEM) images of the initial disbond (5 mm diameter), porosity and voids in the adhesive taken from the adhesion disbond specimen (AD-F2)

In the traditional fatigue debonding growth rate vs. maximum strain energy release rate plot (da/dN vs. G_{max}), different groups of data are owing to the mode ratio change (mode I, II and mixed mode). However, when plotted against the normalised g_{max}, all data collapsed in a band and can be represented by a master curve. The difference caused by mode ratio is almost diminished. The variation and scatters shown in Figure 9 are expected for all fatigue tests. In this study, scatters are caused by: (a) crack went into the adhesive bulk in some specimens, and (b) voids and defects were observed in the carrier cloth that will affect the fatigue resistance.

In Figure 13(b), fatigue debonding growth from semi-circular disbond had already propagated to reach the free edges and formed a 5 mm strip disbond (similar to the initial disbond shape in the narrow width coupon joints). Compared with fatigue debonding in the "coupon" joints studied in [25], it can be found that apart from this initial fatigue cycles, fatigue debonding

life of the coupon joint and wider joint do not show much difference. However, coupon joints would provide a very conservative fatigue life prediction (almost one-fourth of that of the wider joint) under the same fatigue crack growth rate (as both joints are bonded by the same adhesive). For the design of larger structure joints, if one uses conventional coupon joint data, it can under-estimate the fatigue life of realistic panel joints that are wider and may contain much smaller disbond that will take longer time to propagate to reach the joint width. Consequently, testing and modelling joints containing smaller semi-circular disbond, and not through the joint width, can better mimic the process induced defects or accidental damage.

6 Conclusions

Fatigue crack growth behaviour from a semi-circular disbond in a lap joint bonded with FM®94 adhesive was investigated. Ultrasound inspection was used to monitor the early stage crack growth behaviour until it reached the joint width. Fatigue life was predicted by finite element modelling in conjunction with the debonding growth rate of adhesive material as function of a normalised strain energy release rate. Modelling the strain energy release rate distribution and observing the debonding evolution have brought a better understanding of the fatigue debonding behaviour and assessed fatigue life prediction for realistic damage scenarios. Based on this study, following conclusions can be drawn:

1. Fatigue debonding growth rates at mixed mode ratio smaller than 0.5 are very close to the mode I values. This is owing to the support carrier cloth attached to the FM®94 adhesive, which effectively resisted the mode II debonding.
2. Using the proposed governing parameter of normalised strain energy release rate, a master trend curve can be established in the form of the Paris law, which covers all the single and mixed mode crack growth rate data with much smaller scatter. Using this master curve and modelling either cohesion or adhesion debonding, predicted fatigue life covers the upper and lower bounds of test measured fatigue life.
3. Fatigue life obtained by testing a conventional coupon joint with a strip disbond is overly conservative for representing fatigue life of realistic structural joint containing much smaller disbond damage. Suggestion is given to use wider joints containing semi-circular disbond for testing and modelling fatigue behaviour of process-induced defects and accidental impact damage.

Acknowledgement

This research is funded by Coventry University, Faculty of Engineering, Environment and Computing, through a PhD studentship to Yiding Liu.

References

[1] Yang S, Gu L, Gibson R. Nondestructive detection of weak joints in adhesively bonded composite structures. Compos Struct 2001;51:63–71.

[2] Mancusi G, Ascione F. Performance at collapse of adhesive bonding. Compos Struct 2013;96:256–61.

[3] de Moura MFSF, Daniaud R, Magalhães AG. Simulation of mechanical behaviour of composite bonded joints containing strip defects. Int J Adhes Adhes 2006;26:464–73.

[4] Karachalios E, Adams R, Da Silva L. Strength of single lap joints with artificial defects. Int J Adhes Adhes 2013;45:69–76.

[5] Guo X, Guan Z dong, Nie H chang, Tan R ming, Li Z shan. Damage tolerance analysis of adhesively bonded composite single lap joints containing a debond flaw. J Adhes 2017;93:216–34.

[6] Sahoo PK, Dattaguru B, Manjunatha CM, Murthy CRL. Fatigue de-bond growth in adhesively bonded single lap joints. Sadhana - Acad Proc Eng Sci 2012;37:79–88.

[7] Elhannani M, Madani K, Legrand E, Touzain S, Feaugas X. Numerical analysis of the effect of the presence, number and shape of bonding defect on the shear stresses distribution in an adhesive layer for the single-lap bonded joint; Part 1. Aerosp Sci Technol 2017;62:122–35.

[8] Liu Y, Lemanski S, Zhang X. Parametric study of size, curvature and free edge effects on the predicted strength of bonded composite joints. Compos Struct 2018; 202: 364–373.

[9] ASTM D3165. Strength properties of adhesives in shear by tension loading of single-lap-joint laminated assemblies. vol. 07. 2014.

[10] Oxford advanced Surface. Onto^{TM} SB1050 : Adhesion promotion of polyurethane and epoxy adhesives. 2015.

[11] Palmieri FL, Belcher MA, Wohl CJ, Blohowiak KY, Connell JW. Laser ablation surface preparation for adhesive bonding of carbon fiber reinforced epoxy composites. Int J Adhes Adhes 2016;68:95–101.

[12] Kanerva M, Saarela O. The peel ply surface treatment for adhesive bonding of composites: A review. Int J Adhes Adhes 2013;43:60–9.

[13] Phariss MKM, Flinn BD, Ballien B, Grace W, Van Voast P. Evaluation of peel-ply materials on composite bond quality. In: Proceedings of the international SAMPE technical conference, Seattle, USA, Oct 31-Nov 3. 2005.

[14] Baker A, Gunnion A, Wang J. On the certification of bonded repairs to primary composite aircraft components. J Adhes 2015;91:4–38.

[15] Davis MJ, McGregor A. Importance of failure mode indentification in adhesive bonded aircraft structures and repairs. ISASI Aust Saf Semin Canb Erra 2010:1–12.

[16] Cawley P. Non-destructive testing—current capabilities and future directions. Proc Inst Mech Eng Part L J Mater Des Appl 2001;215:213–23.

[17] Azari S, Papini M, Spelt JK. Effect of adhesive thickness on fatigue and fracture of toughened epoxy joints - Part I: Experiments. Eng Fract Mech 2011;78:153–62.

[18] Zavatta N. Influence of adhesive thickness on adhesively bonded joints under fatigue

loading. PhD thesis. 2015.
[19] Azari S, Papini M, Spelt J. Effect of surface roughness on the performance of adhesive joints under static and cyclic loading. J Adhes 2010;86:742–64.
[20] ASTM Standard E647−13. Standard test method for measurement of fatigue crack growth rates. ASTM B Stand 2016;03:1–49.
[21] Bürger D, Rans CD, Benedictus R. Characteriztion of Mixed-Mode Fatigue Failure on Metallic Bonded Joints. 27th ICAF Symp., 2013, p. 5–7.
[22] Pascoe J, Alderliesten R, Benedictus R. Methods for the prediction of fatigue delamination growth in composites and adhesive bonds – A critical review. Eng Fract Mech 2013;112:72–96.
[23] Rans C, Alderliesten R, Benedictus R. Misinterpreting the results: How similitude can improve our understanding of fatigue delamination growth. Compos Sci Technol 2011;71:230–8.
[24] Yao L, Sun Y, Guo L, Zhao M, Jia L, Alderliesten RC, et al. A modified Paris relation for fatigue delamination with fibre bridging in composite laminates. Compos Struct 2017;176:556–64.
[25] Liu Y, Lemanski S, Zhang X, Ayre D, Yazdani H. A finite element study of fatigue crack propagation in single lap bonded joints with process-induced disbond. Int J Adhes Adhes 2018;87:1–18.
[26] Paris P, Erdogan F. A critical analysis of crack propagation laws. J Basic Eng 1963;85:528.
[27] Doucet J, Zhang X, Irving P. Fatigue modelling of aluminium plates reinforced with bonded fibre metal laminates. Int J Struct Integr 2013;4:416–28.
[28] ASTM D5528-01. Standard test method for mode I interlaminar fracture toughness of unidirectional fiber-reinforced polymer matrix composites 1. Am Stand Test Methods 2014;03:1–12.
[29] Bernasconi A, Jamil A, Moroni F, Pirondi A. A study on fatigue crack propagation in thick composite adhesively bonded joints. Int J Fatigue 2013;50:18–25.
[30] Cheuk P, Tong L, Wang C, Baker A, Chalkley P. Fatigue crack growth in adhesively bonded composite-metal double-lap joints. Compos Struct 2002;57:109–15.

Experimental and numerical study of the effects of process-induced disbond on fatigue debonding in composite joints

Yiding Liu[a], Xiang Zhang[a,*], Stuart Lemanski[a], Hamed Yazdani Nezhad[b], David Ayre[b]

[a] Faculty of Engineering, Environment and Computing, Coventry University, CV1 5FB, United Kingdom

[b] Enhanced Composites and Structures Centre, School of Aerospace, Transport and Manufacturing, Cranfield University, MK43 0AL, United Kingdom

[*] Corresponding author. Email address: xiang.zhang@coventry.ac.uk

Abstract

Laboratory coupon joints for fatigue debonding tests usually have narrow width and a through-width initial disbond. However, realistic structural joints are much wider and may contain process-induced defects and accidental damage; both are much smaller than the joint width. Small and discrete damage may behave differently from the idealised through-width disbond crack. This has brought a question on whether the laboratory coupon joint can accurately represent the fatigue behaviour of wider structural joints. This paper presents an experimental and numerical study of fatigue behaviour of a wide bonded lap joint with a process-induced defect of semi-circular shape. Fatigue debonding propagation was monitored by ultrasound inspection. Fatigue life was predicted using a normalised strain energy release rate parameter calculated by finite element method, and the adhesive material fatigue crack growth rate data measured under single and mixed mode conditions. Simulation of process-induced defect and validation by experiments have brought a better understanding of fatigue debonding behaviour in wide joints containing realistic damage. Suggestions are given for fatigue fracture tests of bonded joints.

Keywords: adhesive bonding; disbond; composites; finite element analysis; fatigue life prediction

1. Introduction

The use of adhesive bonded joints in Carbon Fibre Reinforced Polymer (CFRP) composites in the aerospace and civil engineering sectors continues to increase. The benefits of using bonded joints over mechanically fastened joints include weight savings, no stress concentration from fastener holes and more uniform load transfer. To ensure the structural integrity of adhesive bonded joints, accurate prediction of fatigue crack growth rate and life is required; relationship of fatigue crack growth life vs. service load history is used to determine the inspection regimes. However, process-induced defects and accidental damage can have different shapes and in different locations [1], all of which affect the joint integrity [2] and

prediction accuracy. Variations of the adhesive damage modes (adhesion or cohesion failure, and combinations of them) also pose challenges to the predictive models.

Most of the laboratory tests were contemplated on coupon size joints (e.g. 25 mm width) with a starter disbond of through-width strip shape. De Moura et al. [3] studied composite lap joint finding that the joint strength was not affected by a strip disbond located in the middle of the joint overlap. Karachalios et al. investigated the effect of rectangular and circular disbond shapes located in the middle of the overlap on the static strength of steel joints [4]. In the case of small disbond, the shape of disbond does not affect the strength; as the disbond size gets bigger, more rapid decrease in the joint strength is found. Guo et al. analysed the effects of through-width disbond at three different locations on the failure strength and failure mode of composite single lap joints, and found that disbond at the edge of the joint overlap region changes the damage initiation pattern, whereas disbond located at quarter of the lap length accelerated the damage growth to the lap edge [5]. Sahoo et al. studied fatigue debonding of an aluminium joint with a strip disbond of 3 mm width at one end of the bond overlap [6]. Fatigue crack growth rate (FCGR) was predicted using the strain energy release rate (SERR) calculated by finite element analysis (FEA). Elhannani et al. investigated the effect of position, number and shape of adhesive disbond on the shear stress distribution in the adhesive layer by finite element modelling [7]. It is found that when the disbond is in the middle of the overlap, interlaminar shear stresses change little as the stress values here are very low. However, if the disbond is present at the free edge of the bond, it causes very high interlaminar shear stresses. In terms of the disbond shape, circular disbond causes higher stress in the adhesive layer. Therefore, it is more dangerous if a circular disbond exists near the free edges of the bond region.

We have previously studied the fracture behaviour of single lap joints in two configurations: (i) a conventional joint width with a through-width stripe disbond as damage starter, (ii) a wider joint with a semi-circular disbond at the free edge of the bond overlap, where debonding between the adherend and adhesive is likely to occur [8]. In reality, manufacture or service induced damages are unlikely to be through the width of the joint, and the free edge locations are more critical than the middle region. Calculated strain energy release rate distributions along or around the front of a starter damage for the mentioned two joint configurations were calculated as shown in Figure 1, which are very different from each other. For the through-width stripe disbond, normalised mode I and mode II SERR distributions are

almost flat along the defect front apart from sudden jump at the free edges, indicating a uniform crack propagation front. For the semi-circular disbond, the mode I SERR at the crack mouth is much higher that will drive the crack to propagate along the joint width direction first; it can take a long time to propagate the starter defect to the free edges if the width of the joint is sufficiently wide. It is therefore important to develop models to predict wider joint performance under cyclic loads with realistic starter defects in terms of shape and location. So far, to the best knowledge of the authors, there is no published work on the propagation of embedded disbond similar to the configuration of Figure 1(b) for adhesive bonded joints under fatigue loads by experiment or modelling.

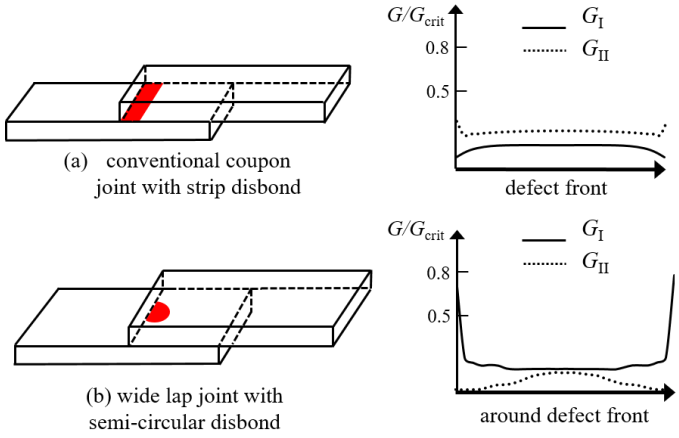

Figure 1: Distribution of SERR for: (a) conventional coupon joint with a through-width strip disbond, and (b) wide lap joint with a semi-circular disbond.

In addition to purposely embedded disbond [3–7], defects can exist inside the adhesive bulk as well as at the adherend-adhesive interface. This paper presents an experimental and numerical investigation of fatigue behaviour of a wide composite lap joint with an idealised disbond starter of semi-circular shape in the adhesive bulk and also at the adherend-adhesive interface. Fatigue testing was conducted and debond propagation was monitored by ultrasound inspection. Fatigue debonding was also modelled in a two-step analysis: a) computing the strain energy release rate by the Virtual Crack Closure Technique (VCCT) under quasi-static load with a crack extension scheme; b) calculating fatigue debonding rate by a normalised strain energy release rate representing the combination of single and mixed modes of the debonding driving force (i.e. SERR) and fatigue debonding growth rate property the adhesive material. Fatigue life is then predicted and compared with experimental results of both conventional and wide coupon joints.

2. Experimental

2.1 Materials and specimens

Composite adherends of 2 mm thickness were manufactured from unidirectional Hexcel® IM7/8552 carbon fibre epoxy pre-preg with quasi-isotropic stacking sequence of $[0/45/90/-45]_S$. The geometry and dimensions of wide lap joint, as shown in Figure 2, were proportionally adopted from ASTM standard D3165 [9]. The adherends were bonded by Cytec FM® 94 modified epoxy adhesive film, which is a moisture resistant adhesive designed for use in high temperature environment. The nominal thickness is 0.25 mm including the polyster carrier cloth. The joints are assembled using secondary bonding process with two cured composite plates curing with the adhesive together. An artificial disbond of semi-circular shape was cut off from a 0.025 mm thickness Teflon® release film using a circular punch and embedded in the front. To ensure high surface quality during the bonding process, a coupled surface treatment was used; application of peel ply followed by pre-treatment with Onto™ SB 1050 supplied by Oxford Advanced Surfaces [10] to introduce chemical bonding interactions, since peel ply alone cannot ensure a perfect quality bond and may not necessarily satisfy initial airworthiness requirements [11–14]. The joint specimens were cured at 120 ºC for 40 minutes. A constant pressure of 0.28 MPa was uniformly applied using a clamping plate with fasteners (see Figure 2(c)). Debonding cracks were monitored from the four corners of the joint overlap area, which are denoted as A and B (at the runout end with artificial disbond), C and D (the opposite end without artificial disbond), as shown in Figure 2(b).

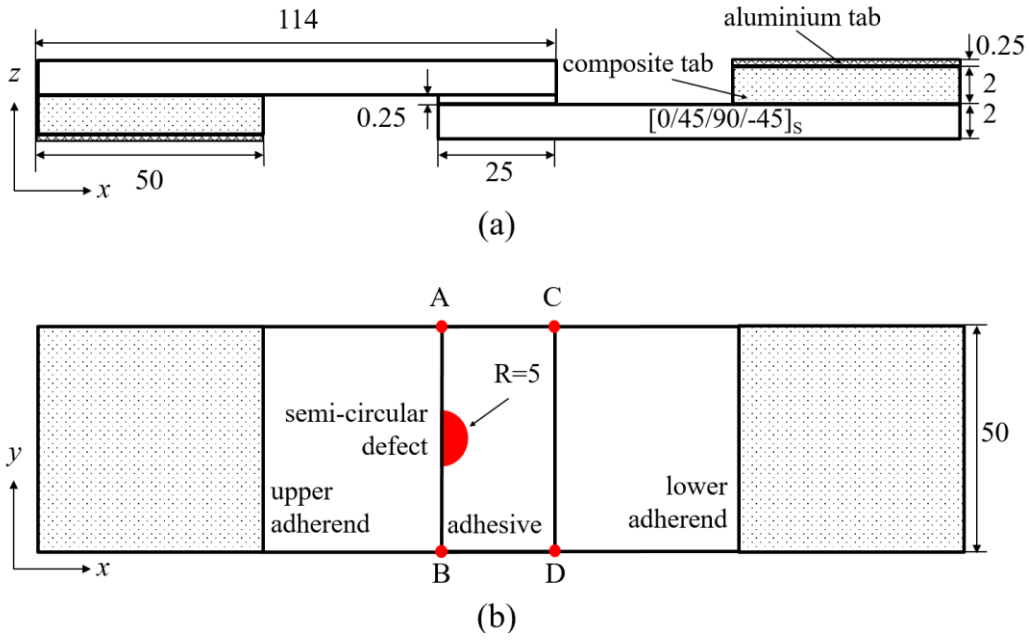

(c) (d)

Figure 2: Wide lap joint used in this study: (a) side view, (b) top view showing a semi-circular initial disbond; geometry and dimensions are adopted from [9] (unit: mm). Fatigue cracks were monitored from the four corners of the adhesive bond, marked as A, B, C, D. (c) clamping plates with fasteners to ensure uniform adhesive thickness, (d) fatigue experiment setup

2.2 Types of initial disbond

Adhesive debonding may be caused by either cohesion failure (fracture within the adhesive bulk) or adhesion failure (interfacial failure between adhesive and adherend) [15]. Cohesion failure found in service is typically a design issue, e.g. insufficient overlap length or excessive peel stress, or excessive porosity, e.g. due to exposure of pre-cured adhesive film to high humidity. Adhesion failure occurs as a direct result of the manufacturing quality, e.g. inappropriate surface preparation or ineffective surface treatment process (a chemically inactive surface).

To replicate these two damage scenarios in laboratory tests, two different types of initial disbond were embedded in the specimens. Adhesive disbond was inserted in the adherend-adhesive interface using one layer of adhesive (referred as "AD specimen", Figure 3(a)). Cohesive disbond was inserted between two adhesive layers (referred as "CD specimen", Figure 3(b)). It is worth noting that the nominal thickness of these specimens was almost the same regardless of adhesive disbond or cohesion disbond as the two adhesive layers were melted into each other during the curing cycle (measured adhesive thickness was 0.37 mm for adhesion disbond (AD) and 0.42 mm for cohesion disbond (CD) after curing). This is considered to be caused by the presence of carrier cloth in the adhesive, which acts as a spacer between the adherends during curing and it is effective at controlling the bondline thickness. Care was taken to ensure that the cohesion disbond remained in the adhesive bulk and not repositioned to the adherend-adhesive interface after the curing process.

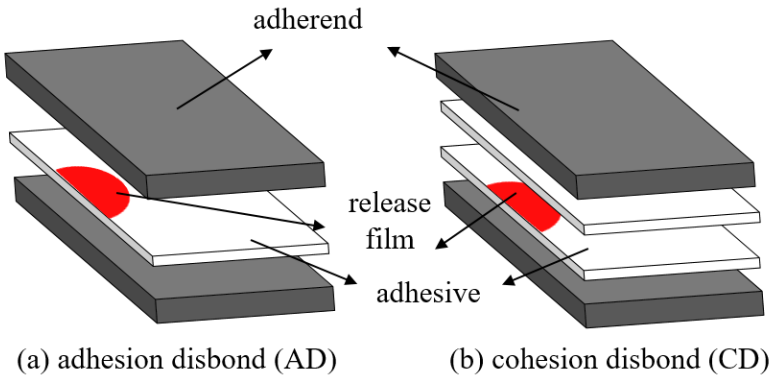

Figure 3: Schematic of designed disbonds: (a) adhesion disbond (AD) inserted at the adhesive-adherend interface, (b) cohesion disbond (CD) embedded between two adhesive layers and cured within the adhesive bulk.

2.3 Fatigue tests and results

Fatigue tests were conducted under constant amplitude load on a DMC servo-hydraulic tester with a 20 kN load cell (see Figure 2(d)). The maximum applied load 8.46 kN was at 50% of the static failure load. The cyclic load ratio was 0.1 and the test frequency was 3 Hz. Two specimens of each disbond type were tested, named as CD-F1, CD-F2 and AD-F1, AD-F2.

2.3.1 Crack growth monitoring

Crack growth was monitored by ultrasound C-scanning at selected test intervals before it reaches the joint free edges. After running test for the initial 3×10^4 cycles, the specimen was removed from the test machine for ultrasound inspection and then realigned to the machine to continue another 5×10^4 cycles. The inspection intervals were adjusted according to the damage propagation observed from previous C-scan. To avoid alteration of realignment, a specimen centreline was marked.

Once the debonding had reached the joint free edge(s), crack lengths were measured from the four corners of the joint overlap (A, B, C, D position in Figure 2) using a travelling optical microscope equipped with a digital camera. To observe the crack profile, fatigue test was interrupted a few times with static tension load being maintained to open the crack, and red ink was manually injected through a needle nozzle through the interface of the overlap. It allows the liquid to flow to the disbond area for post-failure identification of the crack propagation profile. This is similar to the dye penetrant technique used in the aerospace and other industries, which does not influence the crack propagation rate [16].

Figure 4 illustrates ultrasonic C-scan results of (a) adhesion disbond specimen (AD-F1) after 5×10^4, 1×10^5 and 1.7×10^5 cycles, (b) cohesion disbond specimen (CD-F1) after 8×10^4,

1.4×10^5 and 2.4×10^5 cycles compared with the initial disbond profile before testing. The dark red colour indicates strong signal suggesting good bond (the small signal variation in the dark red region is the result of non-uniform adhesive thickness). The black colour typifies the disbond that absorbed all ultrasound signals. Measured crack lengths in the transverse and concentric directions ($2a_1$ and a_2, respectively) are presented in Table 1.

The C-scan results indicate significant scatters in laboratory tests of composite lap joints. By comparing the images taken at various intervals, an evident crack growth in the transverse direction could be observed, which speedily extended to the joint free edges for the adhesion type initial disbond. It can be seen that crack also grew in the concentric direction at the early cycles, although the growth rate is much slower than that in the transverse direction. Similar crack growth pattern was also observed for the cohesion disbond, however, crack propagated gradually in both directions. This suggested that fatigue damage mainly evolves in the transverse direction (i.e. perpendicular to the loading direction) until reaching the joint width.

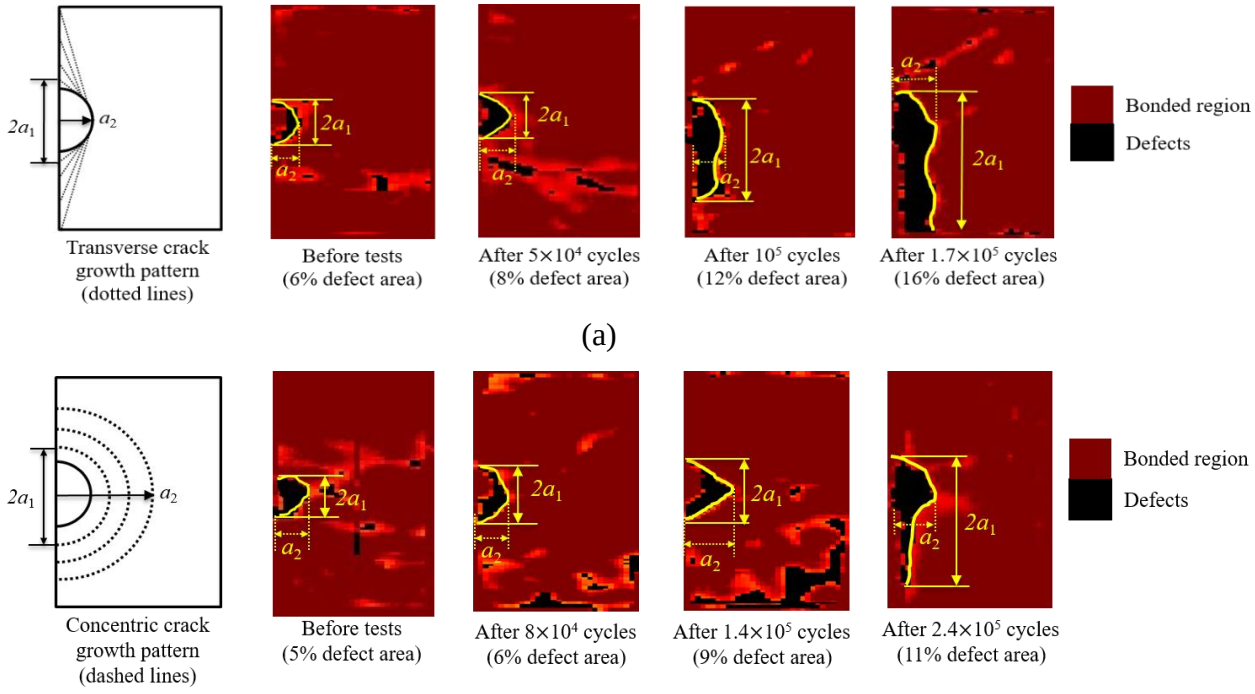

Figure 4: C-scan images of crack growth profiles for (a) adhesion disbond (specimen AD-F1) at 5×10^4, 1×10^5 and 1.7×10^5 load cycles, (b) cohesion debond (CD-F1) at 8×10^4, 1.4×10^5 and 2.4×10^5 cycles.

Table 1 Measured crack lengths in transverse and concentric directions according to C-scan results (unit: mm)

	Adhesion disbond, Specimen F1 (AD-F1)				Cohesion disbond, Specimen F1 (CD-F1)			
	Initial debond size	5×10^4 cycles	1×10^5 cycles	1.7×10^5 cycles	Initial debond size	8×10^4 cycles	1.4×10^5 cycles	2.4×10^5 cycles

Transverse direction ($2a_1$)	9.2	11.2	21.9	29.3	8.5	10.0	11.3	23.5
Concentric direction (a_2)	4.4	5.1	5.3	7.5	4.9	5.2	6.6	6.8

Note: for the transverse and concentric crack profiles, see sketch in Figure 4.

2.3.2 Fatigue crack growth life

Figure 5 plots the monitored crack length (a) measured from four corners (A, B, C, D) with respect to number of cycles (N) for cohesion-disbond ((a) CD-F1 and (b) CD-F2) and adhesion-disbond ((c) AD-F1 and (d) AD-F2) specimens. For all specimens, main cracks were observed from corners A and B, whereas minor cracks were discovered at corners C and D after some period as a result of secondary bending. Crack growth rate was approximately the same for corners A and B, indicating that crack front has already become uniform when the crack could be observed from corners A and B, and later from corners C and D.

Fatigue crack growth rate in composite lap joints show a significant difference between cohesion and adhesion disbonds. The fatigue load cycle curve of the cohesion disbond (CD) is apparently gradual until 6×10^5 to 8×10^5 cycles, while that of the adhesion disbond (AD) is rapid ultimately failing at 4.5×10^5 cycles, representing 40% reduction in fatigue life. Literature also showed significant scatter between the two types of debonding [17], which is one of the main difficulties in implementing a damage tolerance design for adhesive joints. Other published studies [18,19] have suggested that small differences in adhesive thickness have little influence on the fatigue crack growth rate. Therefore, it is reasonable to suggest that the large difference in the fatigue behaviour is related to the different types of disbond starter; crack resulting from cohesion disbond propagates via the cohesion failure mechanism (i.e. fracture within the adhesive layer in the plane of the carrier cloth), as shown in Figure 6(a). In adhesion disbond scenario, it is easier to have an adhesion failure as the starter disbond was inserted between the adherend-adhesive interface, consequently it would require higher energy to propagate into the adhesive bulk causing cohesive failure. This was also observed in the cohesion disbond specimens as the fabric carrier deflected the internal cracks towards the interfaces. However, with the cohesion disbond, theoretically, both cohesion failure and adhesion failure can occur. As the resistance to cohesion failure is much greater than that to adhesion failure, observed damage mode switch during fatigue testing is understandable, i.e., a cohesive crack deviated towards to the adherend-adhesive interface. With this failure mode switch from cohesion to adhesion in the CD specimen, crack would

require higher strain energy to propagate, hence larger number of load cycles comparing to the adhesion disbond specimens.

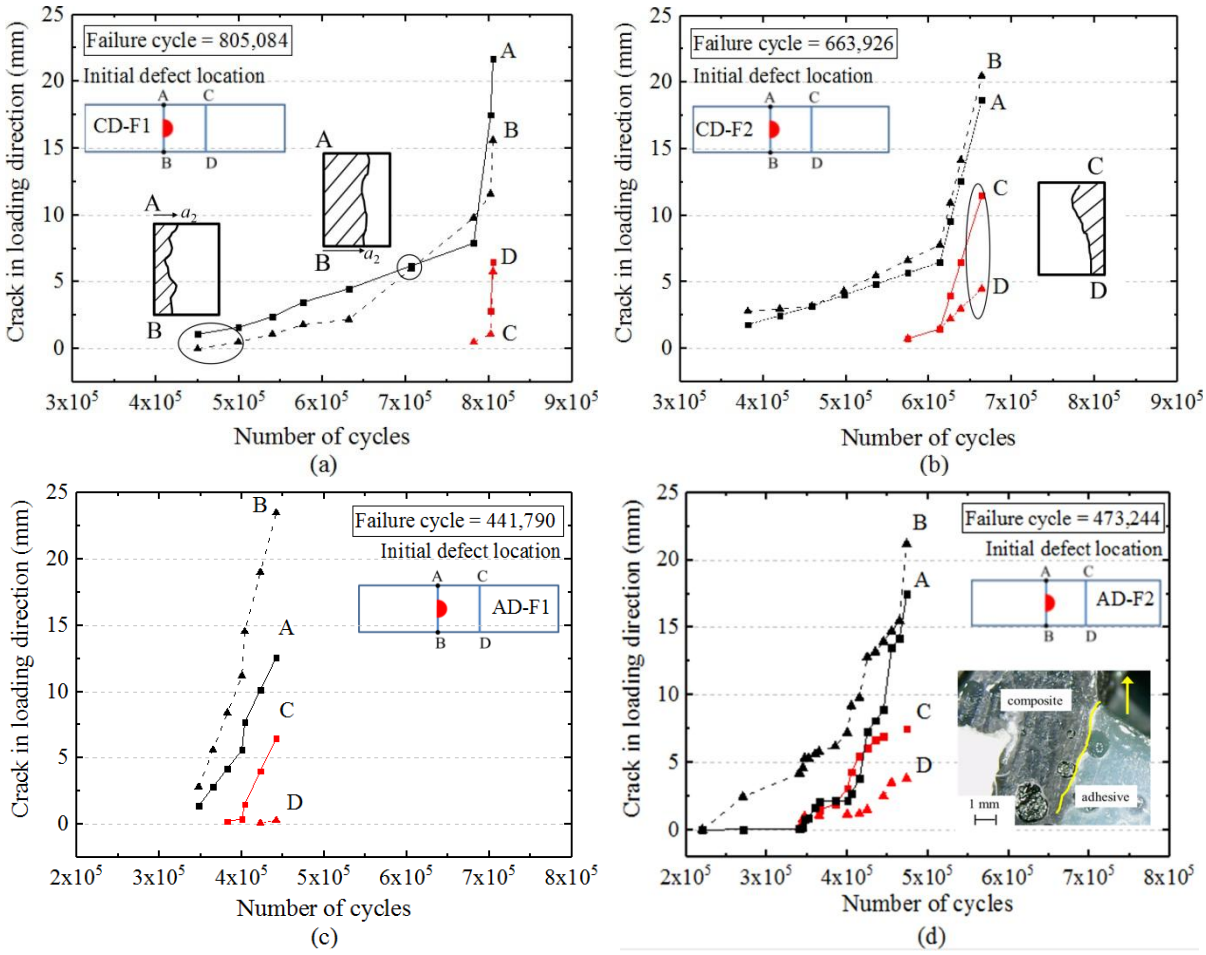

Figure 5: crack lengths in the load direction measured at four corners of overlap (A,B,C,D; a_2 is the main crack from artificial disbond); (a) and (b) show cohesion disbond specimens CD-F1 and CD-F2, (c) and (d) show adhesion disbond AD-F1 and AD-F2; photo insert shows crack from A and B at the maximum cyclic load at 381,718 cycles, yellow line indicates crack propagation path, and arrow points the applied load direction.

2.3.3 Fractography

Fractographic examination was carried out after fatigue testing. Figure 6(a) shows the fracture surfaces of a cohesion disbond specimen (CD-F2) with red ink marked interface. The left interface represents the crack propagation after 541,876 cycles. The shape of the ink mark supports the assertion that the crack front has rapidly elongated to the joint free edges and that by this stage the crack has become a uniform full-width disbond of about 9 mm length. A mixed adhesion-cohesion failure was observed for CD-F2. Fractography of adhesion disbond specimen (AD-F2) without red ink insertion is shown in Figure 6(b) illustrating adhesion failure dominance. Delamination in adherend is also observed in AD-F2.

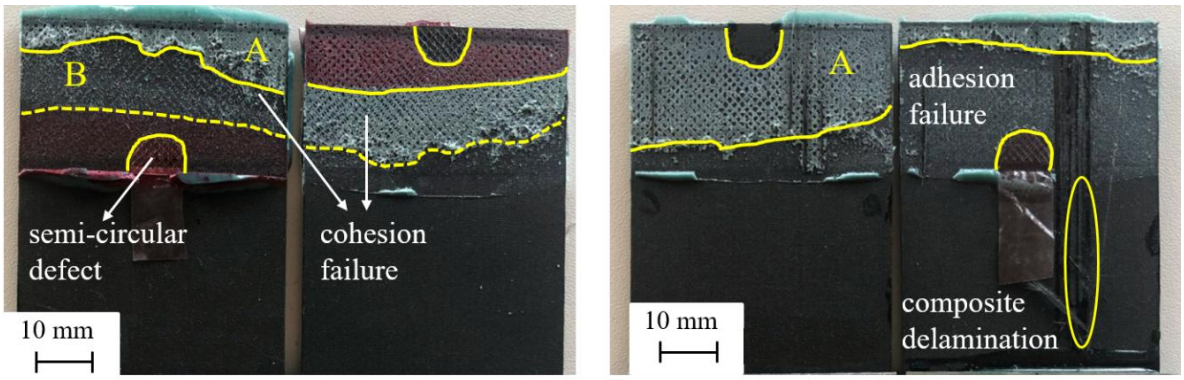

(a) (b)

Figure 6: Fracture surfaces of (a) cohesive disbond specimen (CD-F2) in mixed adhesion-cohesion failure; red ink indicates a full-width crack of 9 mm at 541,876 cycles, (b) adhesion disbond specimen (AD-F2), adhesion failure and delamination were observed. Area A is cohesion failure and B is adhesion failure.

2.4 Fatigue crack growth rate property for FM94 adhesive

Predicting the fatigue life of joints requires the adhesive material data in terms of debonding crack growth rates under mixed mode load. In this study, the Double Cantilever Beam (DCB, mode I), Mixed Mode Bending (MMB, mixed mode ratio of 0.5 and 0.75 as defined in Eq. (1)) and three-point End Notch Flexure (ENF, mode II) geometries bonded with the FM®94 adhesive were tested, as shown in Figure 7. The initial disbond was always at the adhesive-adherend interface. Fatigue crack growth rate (FCGR) was calculated from measured a vs. N relation using the 7-point incremental polynomial method in accordance with the ASTM Standard E647 [20]. Our test data are compared with published work in [21], where fatigue tests were conducted on lap joints made of aluminium adherends and FM®94 adhesive under the modes I, II and mixed mode ratio of 0.25 and 0.75.

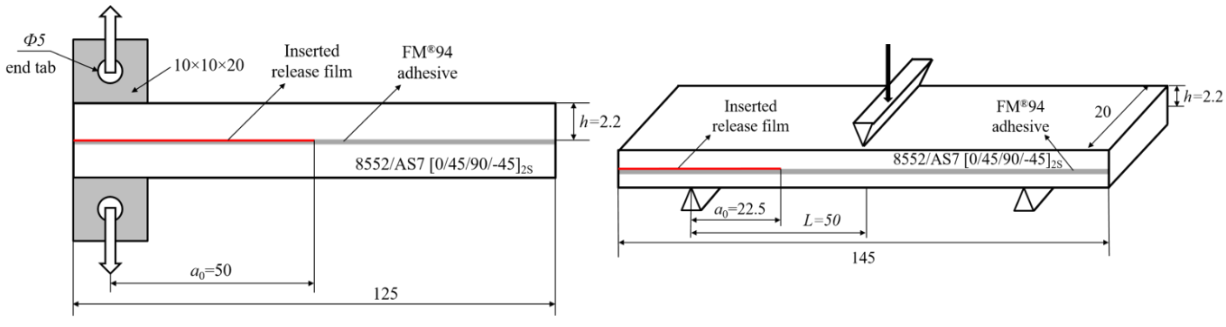

(a) (b)

Figure 7: Dimensions, materials and layup for DCB and three-point ENF specimens (unit: mm). Disbond starter was inserted at the adherend-adhesive interface.

The Paris law type relation based on fracture mechanics has been widely used in the fatigue delamination studies for composites [22] and adhesive joints [23,24]. There is no general consensus on the similitude parameter governing fatigue delamination/disbond growth rate.

Discussion on the importance of using an appropriate governing parameter was made in a previous study by the author [25]. In this current study, a normalised parameter, g_{max}, is used as defined in Eq. (2). It takes account of the effect of the fracture toughness (G_{IC} and G_{IIC}) to reduce the scatter in the fatigue crack growth rate data. The Paris law in Eq. (3) is represented accordingly in Eq. (4):

$$r = \frac{G_{II}}{G_I + G_{II}} \tag{1}$$

$$g_{\max} = \frac{G_{I,\max}}{G_{IC}} + \frac{G_{II,\max}}{G_{IIC}} \tag{2}$$

$$\frac{da}{dN} = C\left(G_{\max}\right)^m \tag{3}$$

$$\frac{da}{dN} = C'\left(g_{\max}\right)^{m'} \tag{4}$$

where $G_{IC,}$ G_{IIC} are the static delamination toughness, also known as the critical strain energy release rate, in mode I and II respectively, C and m are the coefficient and exponent of the traditional Paris law [26], C' and m' are modified Paris law parameters that are determined by fitting the test data.

Figure 8(a) shows measured FCGR of FM®94 adhesive vs. the maximum SERR (G_{max}) measured from single mode and mixed mode coupons. A distinct difference exists between the mode I and mode II, and the fatigue debonding rate data are divided into three zones: mode I dominant (r = 0~0.5), mixed mode (r = 0.5~0.8) where majority data points are inclined to pure mode I, and mode II dominant (r = 0.8~1). Figure 8(b) shows the scanning electron microscope (SEM) images of the fracture surfaces associated with (i) mode I, (ii) mixed mode ratio of 0.5 and (iii) mode II failures of FM®94 adhesive bonded with aluminium substrates [21,27]. For mode I debonding, the micro cracks grow in different directions ahead of the crack tip, and then coalesced to form a main crack. Mode II fracture surfaces contain mainly rollers and vertical cracks. For the mixed mode loading (ratio 0.5), the fracture surface feature is similar to that of the mode I, which substantiates the disbond growth rate being closer to the pure mode I result. The mixed mode behaviour is strongly influenced by the presence of the fibre carrier cloth in FM94, which has higher resistance to the mode II loads, resulting in a reduced mode II fracture than that imposed upon the samples (i.e. by the secondary bending effect).

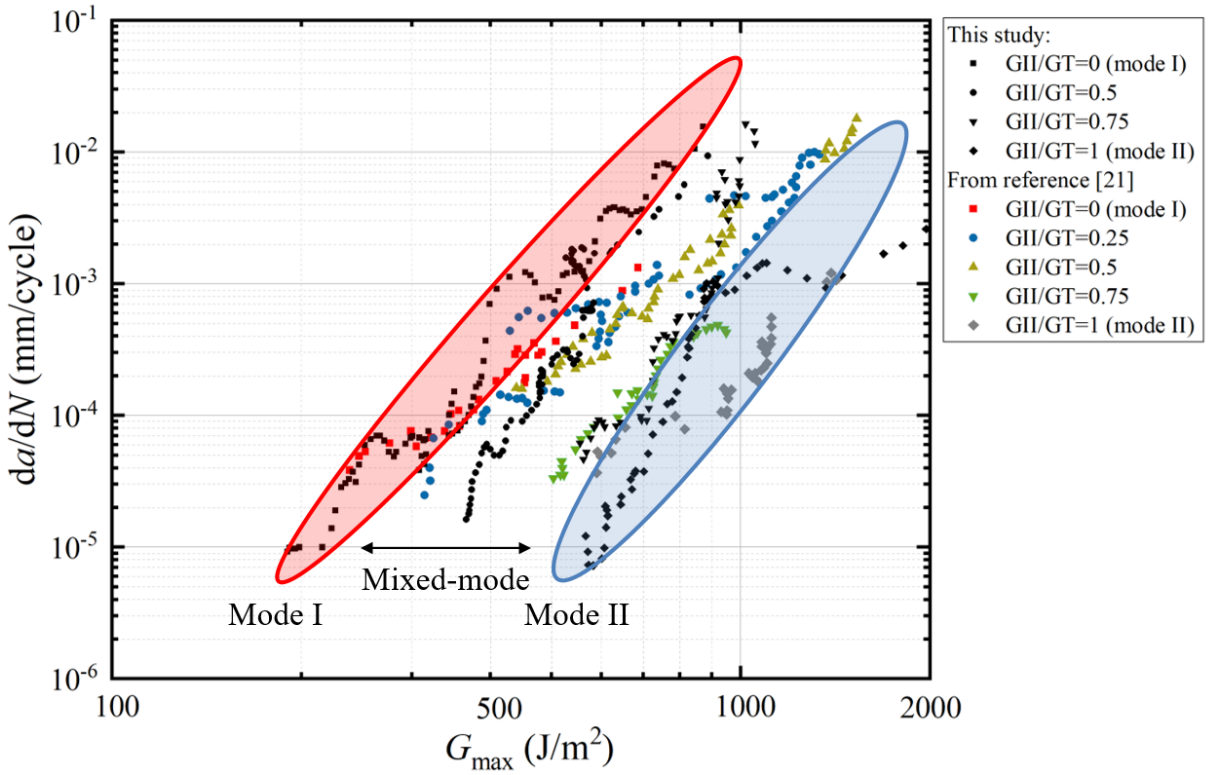

Figure 8(a): Measured fatigue crack growth rate vs. maximum SERR (G_{max}) for FM94 adhesive; filled symbols indicate adhesion debonding by authors of this paper; filled symbols represent cohesion debonding taken from reference [21], using the same adhesive material with aluminium adherends and with initial disbond at the adherend-adhesive interface. G_{max} was calculated using the modified beam theory in [28] at the maximum load with displacement control.

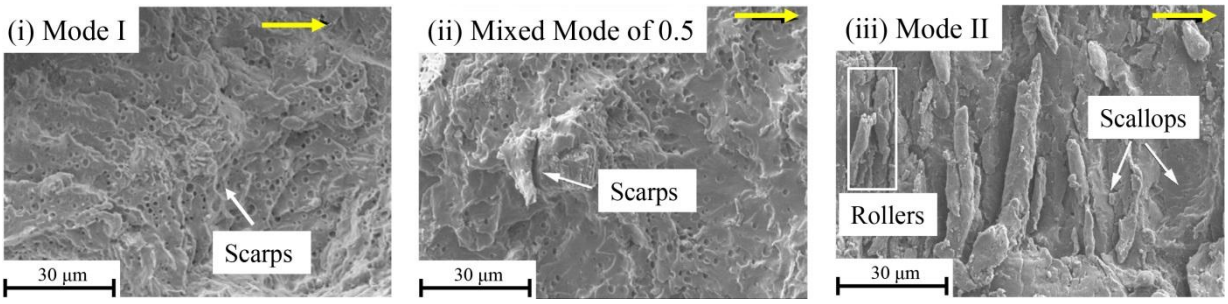

Figure 8(b): Microscopic photos of fracture surfaces of (i) mode I, (ii) mixed mode of ratio 0.5, (iii) mode II, of FM94 with aluminium adherends, adopted from [21]; white arrows indicate characteristics related to different modes; yellow arrows indicate the main crack growth direction.

Figure 9 shows modified plots of FCGR vs. normalised maximum SERR for the same fatigue data as shown in Fig. 8a. For this particular adhesive, it can be seen that majority of the test data at different modes can be covered by a ±35% scatter band so that the best fitted curve can be regarded as a "master curve" that can be described by the Paris law. This linear curve is also a good fit for the pure mode I data in this graph, which may explain why some studies

have used just the mode I data to predict mixed mode crack propagation rate in composite joints [29,30].

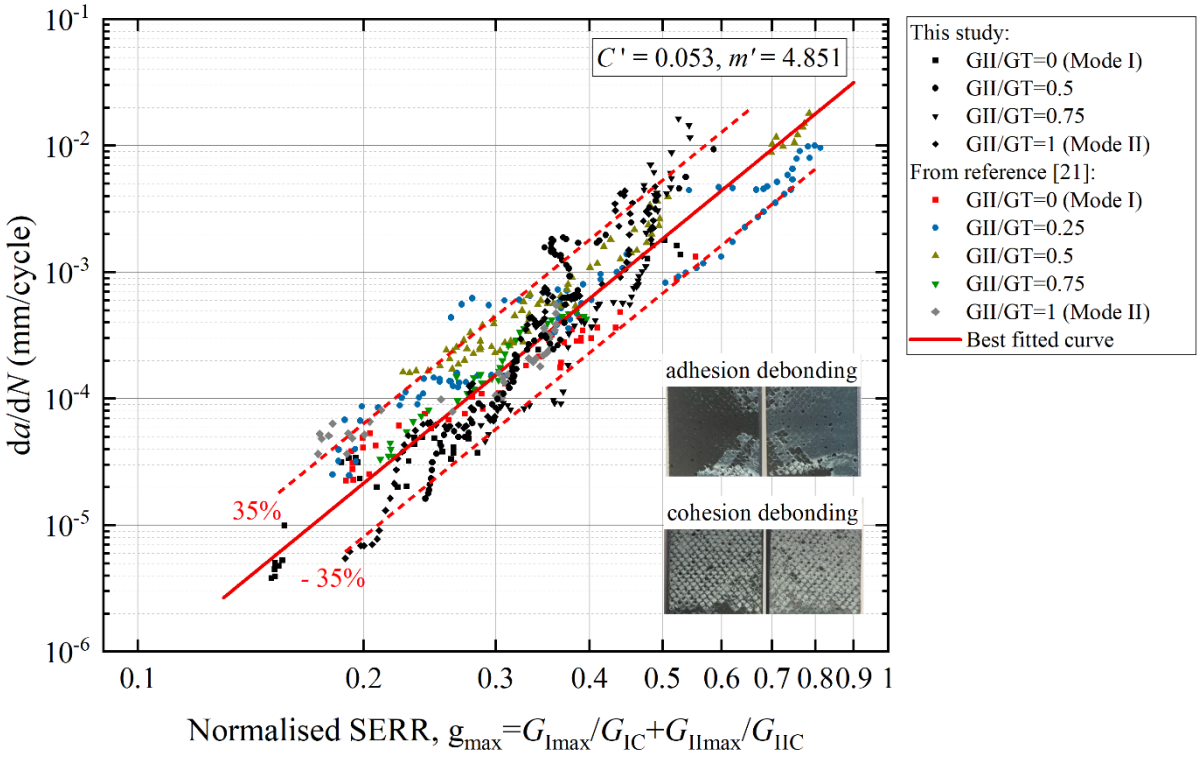

Figure 9: Fatigue crack growth rate vs. normalised SERR (Eq. (2)) of FM94 adhesive for mixed mode tests. Black filled symbols represent adhesion debonding; colour filled symbols are cohesion debonding taken from [21]; red line is the best fitted curve of all test data including data from [21]. Toughness values used: $G_{IC\ (adhesion)}$=867 J/m^2, $G_{IC\ (cohesion)}$=1420 J/m^2, $G_{IIC\ (adhesion)}$=2955 J/m^2, $G_{IIC\ (cohesion)}$=3462 J/m^2, from this study and references [18,21]. Upper and lower boundaries (dash lines) are parallel with the best fitted curve covering majority data points.

3 Modelling approach

3.1 FE model of crack extension

Figure 10 shows the load and boundary conditions of a wide lap joint with a semi-circular disbond. Both the adherends and adhesive were modelled by linear brick elements with incompatible mode (denoted as element C3D8I in ABAQUS code) to enhance the accuracy of bending behaviour. Crack extension was modelled under quasi-static load condition by manually releasing the crack tip nodes in the adherend-adhesive interface and modifying the bonded node set according to a designated pattern. Mesh size of 0.5 mm was used in the bond region based on mesh convergence study. The SERR components were computed using the crack tip node forces and crack opening displacement behind the crack tip. The implicit integration is suitable for debond modelling for computational efficiency and convergence.

By running several FE analyses with different crack lengths and corresponded crack growth profiles, variation of SERR with respect to crack growth profile were calculated.

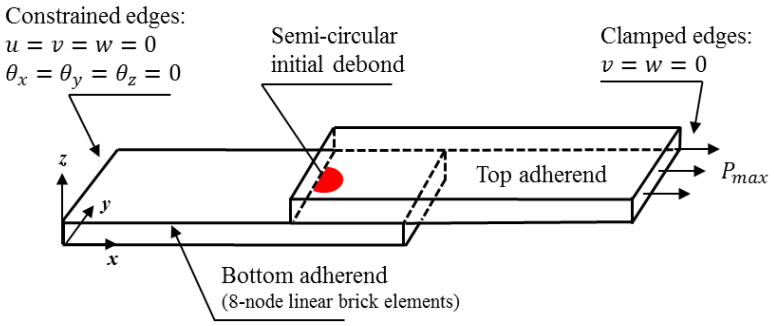

Figure 10: Load and boundary conditions of a wide joint with a semi-circular disbond; the left end were fully constrained, the right end is simply supported with free movement in the x-axis and subjected to a load.

3.2 Strain energy release rate (SERR)

Crack length along the transverse direction before reaching the free edges was defined as a_1. After reaching the free edges, it propagated along the overlap length direction, which was defined as a_2, as shown in Figure 11(a). FE modelling of selected continuous crack growth profiles (a_1 of 5, 6.5, 10.2, 12.4, 17.9 and 20.8 mm based on C-scanning) were performed and the mode I, II and III SERR components (G_{I}, G_{II} and G_{III}) at the crack tip locations were illustrated in Figure 11(b). The assumption of crack propagation along the 0° direction is based on the ratio of the total SERRs at two crack fronts in 0° and 90° directions as the C-scan revealed much slower crack propagation along the concentric directions.

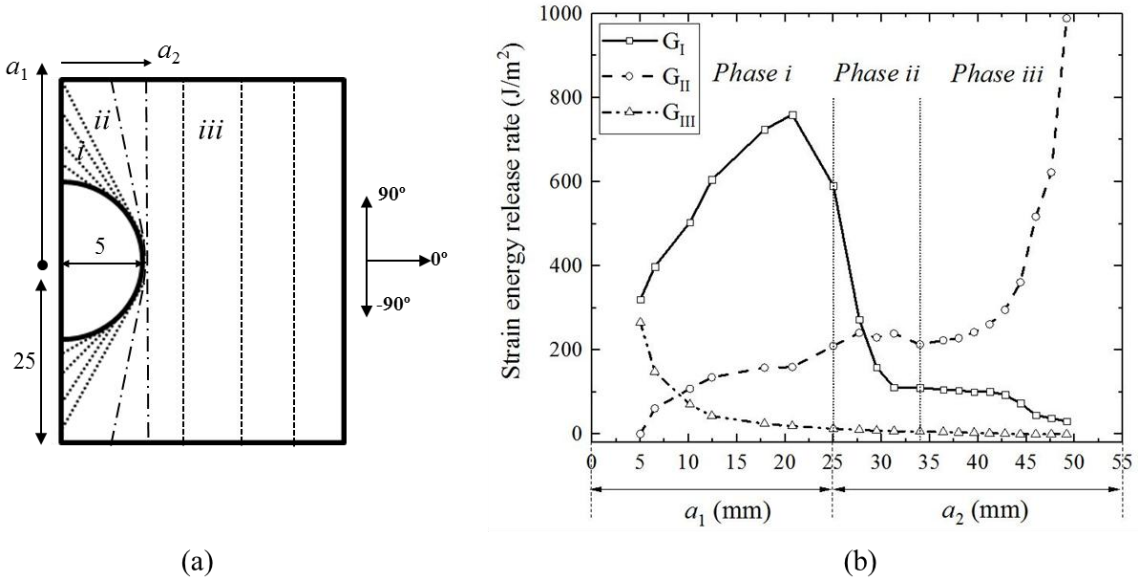

Figure 11: (a) Definition of crack growth profile in three phases (*i*, *ii*, *iii*) in transverse and concentric patterns (unit: mm), (b) mode I, II and III SERR components (G_{I}, G_{II} and G_{III}) vs. crack length (a_1 and a_2) calculated under static maximum load 8.46 kN.

Figure 11(b) shows that three crack propagation phases can be defined by the fracture mode change. In phase *i* (crack extends towards the free edges), G_I keeps increasing due to the free edge stress concentration at the a_1 crack front. G_{III} component exists at the 90° crack tip during phase *i*, which could not be ignored when the crack length was relatively small as the in-plane tension could bring out-of-plane shear deformation. In phase *ii* (crack transferred to a 5 mm strip crack similar to the initial disbond in narrow coupon joint), crack length grew longer and local stress becomes more perpendicular to the crack plane. G_I dropped significantly from 600 J/m^2 to around 150 J/m^2, but G_{II} was almost constant, indicating the dominant fracture mode switching from mode I to mode II as the joint experienced higher shear stress when the crack reached the free edges. G_{III} becomes much smaller than both G_I and G_{II} and can be neglected from Phase ii onwards. In phase *iii* (uniform crack front), G_{II} increased steeply from 200 J/m^2 to more than 1000 J/m^2, whereas G_I decreased significantly to around 20 J/m^2. The contribution of mode II is more important and eventually the crack becomes unstable causing a sudden failure.

3.3 Fatigue life prediction

Fatigue life prediction procedure used in this study is shown in Figure 12. Three parts are involved: (1) basic material property test including the fracture toughness and Paris law relationships for different mixed modes; (2) calculation of the crack growth driving force (SERR components) by FEA, using the model shown in Figure 9. The obtained SERR was then employed to Eq. (2) taking account of two different scenarios of adhesion or cohesion debonding by using the corresponding facture toughness and the master trend line of the crack growth rate data (Figure 9); (3) predict the fatigue crack growth rate and life by numerically integrating the Paris law using cumulative damage algorithm, starting from the initial crack length to the final critical crack length.

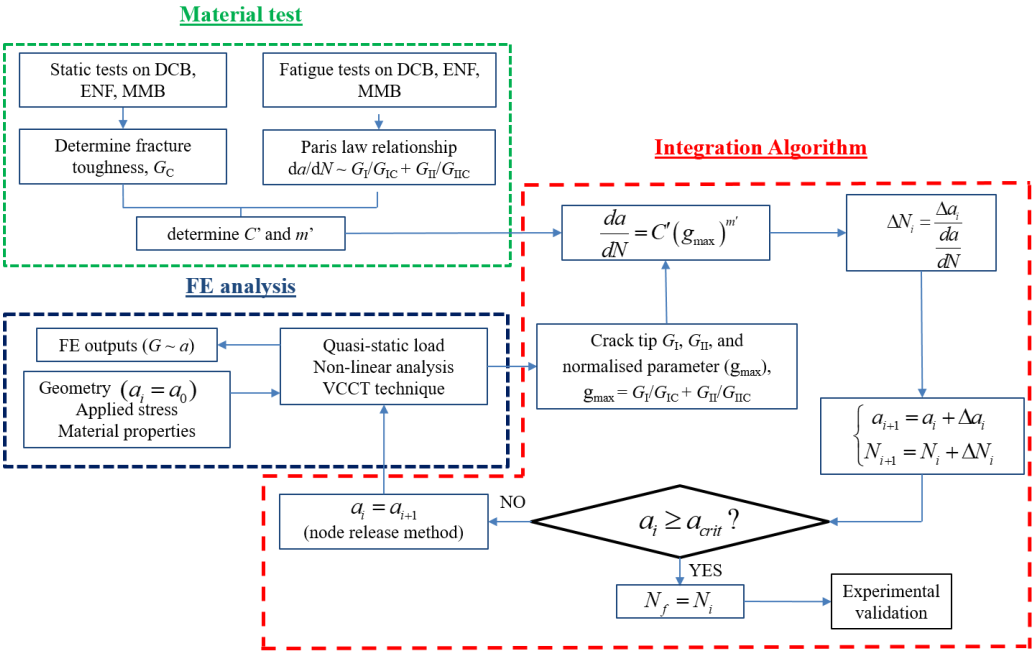

Figure 12: Flow chart of procedures used for fatigue life prediction; three key steps are: material test, FE analysis of crack growth driving force, and numerical integration algorithm for crack growth accumulation.

4 Validation of fatigue life prediction

Predicted crack length (a_1) vs. cycle numbers (N) for the Phase *i* and *iii* and comparison with experimental measurement are presented in Figure 13. For the semi-circular disbond, nearly half of the total fatigue life is spent to propagate the initial disbond to the joint free edges.

In the process of initial disbond propagating to reach the joint width (i.e. Phase *i*), prediction based on cohesion debonding data is more accurate than using the adhesive debonding data, indicating that cohesion damage is the dominant mode in Phase *i*. This model gradually changed into the adhesive debonding mode with further crack propagation, shown by the required larger cycle numbers in the crack prediction, as shown in Figure 13(b) in Phase *iii*). For Phase *iii*, adhesion debonding mode is more efficient compared to cohesion debonding model, indicating the dominance of adhesion failure in this phase.

The cohesion debonding model provides un-conservative life prediction comparing to the adhesion debonding model. This difference could possibly be ascribed to the smaller normalised g_{max} value in the cohesive debonding case due to higher delamination toughness values (G_{IC} and G_{IIC}, see the values in the captions of Figure 9) caused by the carrier cloth, which results in a slower FCGR and longer fatigue life. The adhesion debonding based model has satisfactorily predicted the fatigue life caused by adhesion disbond, whereas the model based on cohesion reproduces the initial stage of the fatigue life of the cohesion disbond more

closely but fails to accurately predict the final failure. This is caused by the cumulative effect of small discrepancies between the experimental tests (Figure 8(a)) and the normalised, fitted data (Figure 9). Therefore, the normalisation to one master trend curve does not accurately predict the fatigue life when the mixed mode ratio is higher than 0.5 in Phase *iii*. However, Phase *iii* is the final stage of crack growth life when the growth rate is faster; therefore, this method still provides qualitative agreement of the behaviour even in these latter stages of crack propagation.

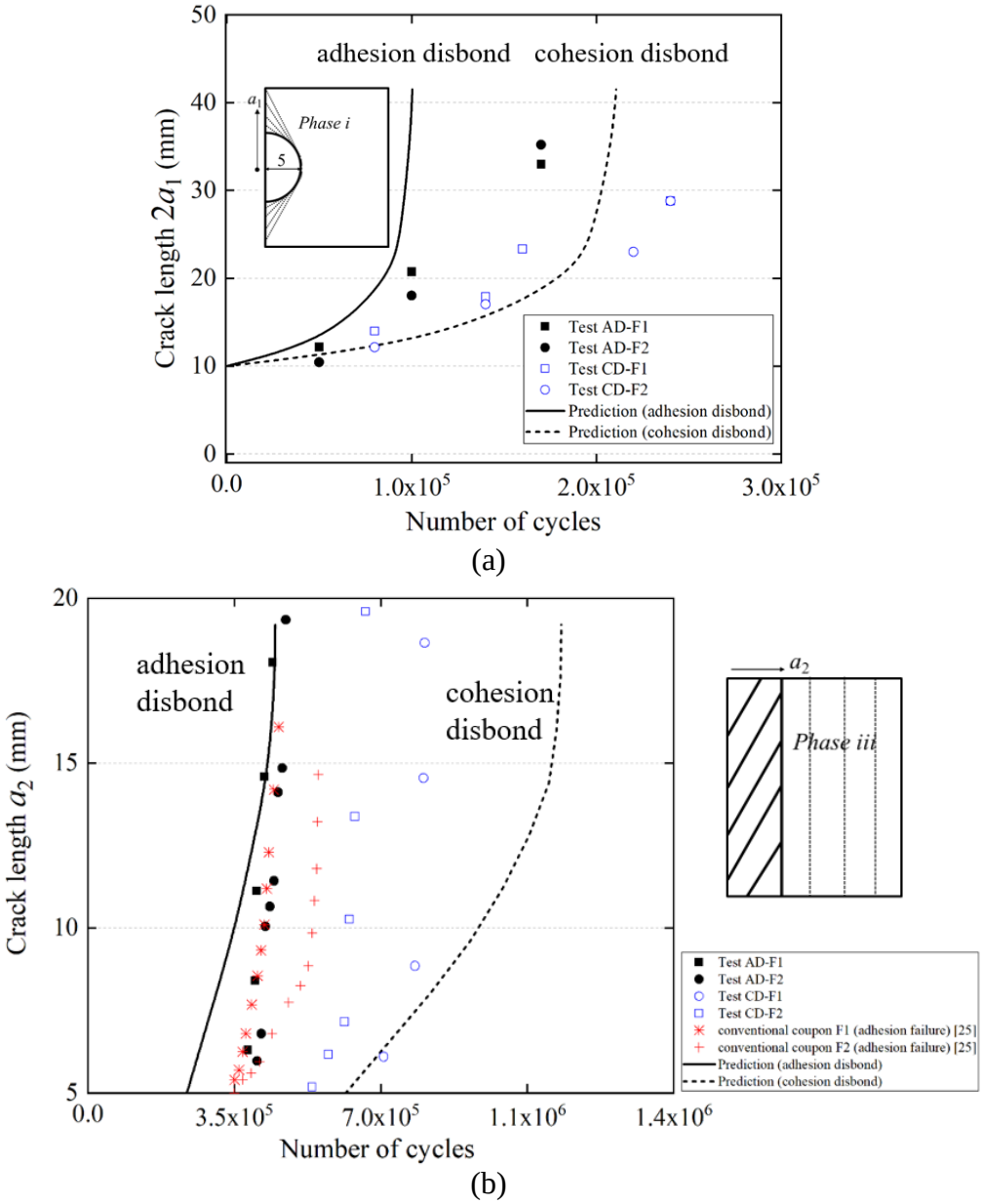

Figure 13: Fatigue crack growth life prediction in (a) Phase *i* (crack configuration a_1) and (b) Phase *iii* (crack configuration a_2), and comparison with test results and conventional coupon joint (adhesion failure) [25].

5 Discussion

The experimental results have shown variations and scatters; for joints with cohesion disbond, fatigue life of the two specimens were 6.7×10^4 and 8.1×10^4 cycles. It is not uncommon in the large scale laboratory fabrication of bonded joints that samples may have localised defects (i.e. due to inappropriate surface preparation or ineffective surface treatment), even though there are bonding quality assurance guidance. Another reason is the porosities and voids in the adhesive, as shown by the Scanning Electron Microscope (SEM) images in the adhesive taken from the adhesion disbond specimen (AD-F2) in Figure 14. Roughly 15% of porosity and void exist in the adhesive (the largest porosity diameter was about 1 mm), which affected the joint fatigue behaviour and caused scatters.

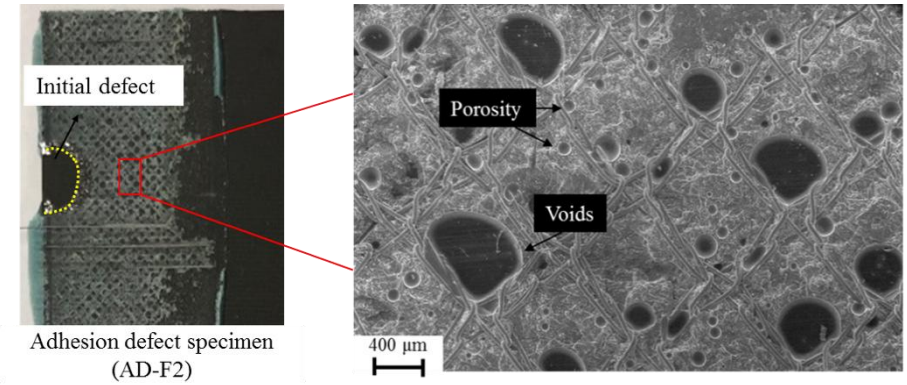

Figure 14: Scanning Electron Microscope (SEM) images of the initial disbond (5 mm diameter), porosity and voids in the adhesive taken from the adhesion disbond specimen (AD-F2)

In the traditional fatigue debonding growth rate vs. maximum strain energy release rate plot ($\mathrm{d}a/\mathrm{d}N$ vs. G_{max}), different groups of data are owing to the mode ratio change (mode I, II and mixed mode). However, when plotted against the normalised g_{max}, all data collapsed in a band and can be represented by a master curve. The difference caused by mode ratio is almost diminished. The variation and scatters shown in Figure 9 are expected for all fatigue tests. In this study, scatters are caused by: (a) crack went into the adhesive bulk in some specimens, and (b) voids and defects were observed in the carrier cloth that will affect the fatigue resistance.

In Figure 13(b), fatigue debonding growth from semi-circular disbond had already propagated to reach the free edges and formed a 5 mm strip disbond (similar to the initial disbond shape in the narrow width coupon joints). Compared with fatigue debonding in the "coupon" joints studied in [25], it can be found that apart from this initial fatigue cycles, fatigue debonding

life of the coupon joint and wider joint do not show much difference. However, coupon joints would provide a very conservative fatigue life prediction (almost one-fourth of that of the wider joint) under the same fatigue crack growth rate (as both joints are bonded by the same adhesive). For the design of larger structure joints, if one uses conventional coupon joint data, it can under-estimate the fatigue life of realistic panel joints that are wider and may contain much smaller disbond that will take longer time to propagate to reach the joint width. Consequently, testing and modelling joints containing smaller semi-circular disbond, and not through the joint width, can better mimic the process induced defects or accidental damage.

6 Conclusions

Fatigue crack growth behaviour from a semi-circular disbond in a lap joint bonded with FM®94 adhesive was investigated. Ultrasound inspection was used to monitor the early stage crack growth behaviour until it reached the joint width. Fatigue life was predicted by finite element modelling in conjunction with the debonding growth rate of adhesive material as function of a normalised strain energy release rate. Modelling the strain energy release rate distribution and observing the debonding evolution have brought a better understanding of the fatigue debonding behaviour and assessed fatigue life prediction for realistic damage scenarios. Based on this study, following conclusions can be drawn:

1. Fatigue debonding growth rates at mixed mode ratio smaller than 0.5 are very close to the mode I values. This is owing to the support carrier cloth attached to the FM®94 adhesive, which effectively resisted the mode II debonding.
2. Using the proposed governing parameter of normalised strain energy release rate, a master trend curve can be established in the form of the Paris law, which covers all the single and mixed mode crack growth rate data with much smaller scatter. Using this master curve and modelling either cohesion or adhesion debonding, predicted fatigue life covers the upper and lower bounds of test measured fatigue life.
3. Fatigue life obtained by testing a conventional coupon joint with a strip disbond is overly conservative for representing fatigue life of realistic structural joint containing much smaller disbond damage. Suggestion is given to use wider joints containing semi-circular disbond for testing and modelling fatigue behaviour of process-induced defects and accidental impact damage.

Acknowledgement

This research is funded by Coventry University, Faculty of Engineering, Environment and Computing, through a PhD studentship to Yiding Liu.

References

[1] Yang S, Gu L, Gibson R. Nondestructive detection of weak joints in adhesively bonded composite structures. Compos Struct 2001;51:63–71.
[2] Mancusi G, Ascione F. Performance at collapse of adhesive bonding. Compos Struct 2013;96:256–61.
[3] de Moura MFSF, Daniaud R, Magalhães AG. Simulation of mechanical behaviour of composite bonded joints containing strip defects. Int J Adhes Adhes 2006;26:464–73.
[4] Karachalios E, Adams R, Da Silva L. Strength of single lap joints with artificial defects. Int J Adhes Adhes 2013;45:69–76.
[5] Guo X, Guan Z dong, Nie H chang, Tan R ming, Li Z shan. Damage tolerance analysis of adhesively bonded composite single lap joints containing a debond flaw. J Adhes 2017;93:216–34.
[6] Sahoo PK, Dattaguru B, Manjunatha CM, Murthy CRL. Fatigue de-bond growth in adhesively bonded single lap joints. Sadhana - Acad Proc Eng Sci 2012;37:79–88.
[7] Elhannani M, Madani K, Legrand E, Touzain S, Feaugas X. Numerical analysis of the effect of the presence, number and shape of bonding defect on the shear stresses distribution in an adhesive layer for the single-lap bonded joint; Part 1. Aerosp Sci Technol 2017;62:122–35.
[8] Liu Y, Lemanski S, Zhang X. Parametric study of size, curvature and free edge effects on the predicted strength of bonded composite joints. Compos Struct 2018; 202: 364–373.
[9] ASTM D3165. Strength properties of adhesives in shear by tension loading of single-lap-joint laminated assemblies. vol. 07. 2014.
[10] Oxford advanced Surface. Onto^{TM} SB1050 : Adhesion promotion of polyurethane and epoxy adhesives. 2015.
[11] Palmieri FL, Belcher MA, Wohl CJ, Blohowiak KY, Connell JW. Laser ablation surface preparation for adhesive bonding of carbon fiber reinforced epoxy composites. Int J Adhes Adhes 2016;68:95–101.
[12] Kanerva M, Saarela O. The peel ply surface treatment for adhesive bonding of composites: A review. Int J Adhes Adhes 2013;43:60–9.
[13] Phariss MKM, Flinn BD, Ballien B, Grace W, Van Voast P. Evaluation of peel-ply materials on composite bond quality. In: Proceedings of the international SAMPE technical conference, Seattle, USA, Oct 31-Nov 3. 2005.
[14] Baker A, Gunnion A, Wang J. On the certification of bonded repairs to primary composite aircraft components. J Adhes 2015;91:4–38.
[15] Davis MJ, McGregor A. Importance of failure mode indentification in adhesive bonded aircraft structures and repairs. ISASI Aust Saf Semin Canb Erra 2010:1–12.
[16] Cawley P. Non-destructive testing—current capabilities and future directions. Proc Inst Mech Eng Part L J Mater Des Appl 2001;215:213–23.
[17] Azari S, Papini M, Spelt JK. Effect of adhesive thickness on fatigue and fracture of toughened epoxy joints - Part I: Experiments. Eng Fract Mech 2011;78:153–62.
[18] Zavatta N. Influence of adhesive thickness on adhesively bonded joints under fatigue

loading. PhD thesis. 2015.
[19] Azari S, Papini M, Spelt J. Effect of surface roughness on the performance of adhesive joints under static and cyclic loading. J Adhes 2010;86:742–64.
[20] ASTM Standard E647−13. Standard test method for measurement of fatigue crack growth rates. ASTM B Stand 2016;03:1–49.
[21] Bürger D, Rans CD, Benedictus R. Characteriztion of Mixed-Mode Fatigue Failure on Metallic Bonded Joints. 27th ICAF Symp., 2013, p. 5–7.
[22] Pascoe J, Alderliesten R, Benedictus R. Methods for the prediction of fatigue delamination growth in composites and adhesive bonds – A critical review. Eng Fract Mech 2013;112:72–96.
[23] Rans C, Alderliesten R, Benedictus R. Misinterpreting the results: How similitude can improve our understanding of fatigue delamination growth. Compos Sci Technol 2011;71:230–8.
[24] Yao L, Sun Y, Guo L, Zhao M, Jia L, Alderliesten RC, et al. A modified Paris relation for fatigue delamination with fibre bridging in composite laminates. Compos Struct 2017;176:556–64.
[25] Liu Y, Lemanski S, Zhang X, Ayre D, Yazdani H. A finite element study of fatigue crack propagation in single lap bonded joints with process-induced disbond. Int J Adhes Adhes 2018;87:1–18.
[26] Paris P, Erdogan F. A critical analysis of crack propagation laws. J Basic Eng 1963;85:528.
[27] Doucet J, Zhang X, Irving P. Fatigue modelling of aluminium plates reinforced with bonded fibre metal laminates. Int J Struct Integr 2013;4:416–28.
[28] ASTM D5528-01. Standard test method for mode I interlaminar fracture toughness of unidirectional fiber-reinforced polymer matrix composites 1. Am Stand Test Methods 2014;03:1–12.
[29] Bernasconi A, Jamil A, Moroni F, Pirondi A. A study on fatigue crack propagation in thick composite adhesively bonded joints. Int J Fatigue 2013;50:18–25.
[30] Cheuk P, Tong L, Wang C, Baker A, Chalkley P. Fatigue crack growth in adhesively bonded composite-metal double-lap joints. Compos Struct 2002;57:109–15.